EVALUATION OF SPATIAL AND TEMPORAL EVAPOTRANSPIRATION USING SATELLITE IMAGERY IN THE CHAO PHRAYA RIVER BASIN

INTRODUCTION

In Thailand, the largest basin is the Chao Phraya River Basin, which covers the north and central region of the Kingdom. The varieties of water use in this basin include agriculture, municipal, and industrial. There is a tendency towards higher water demands than in the past, so significant water storage, such as reservoirs and canals, has been added in the watershed area. On the one hand floods often occur during the rainy season, because there are rain storms and excessive water in the reservoirs. On the other hand, during the dry season there is insufficient water, because water in the reservoirs is released without accurate planning during the rainy season. Thus, improving water resources management is becoming more and more necessary.

The availability of water can be evaluated from evapotranspiration, rainfall, and water balance or water budget studies. Evapotranspiration is an outflow and rainfall is an inflow in water budgets. This dissertation evaluated water budgets using evapotranspiration and rainfall, which were calculated from satellite images and also measured data. Recent remote sensing technological developments in evaluating rainfall and evapotranspiration over large areas have not been applied in Thailand. This technology is interesting to apply in the field of water resources management regarding planning, development and operation.

Remotely sensed data are used for studying the Earth's surface. Current technology allows continuous acquisition of data, regular revisit capabilities (resulting in up-to-date information), broad regional coverage, good spectral resolution (including infra-red bands), good spatial resolution, ability to manipulate/enhance digital data, ability to combine satellite digital data with other digital data, cost-

effective data, map-accurate data, possibility of stereo viewing, and large archives of historical data. Remote sensing helps to record data from remote locations. Satellite data provides timely and detailed information about the Earth's surface, especially in relation to the management of our renewable and non-renewable resources. The advantages of satellite data for many fields include for example; assessment and monitoring of vegetation types and their status, soil surveys, mineral exploration, map making and revision, production of thematic maps, water resources planning and monitoring, urban planning, agricultural property planning and management, crop yield assessment, and natural disaster assessment.

The characteristics of evapotranspiration and rainfall include variable spatial and temporal resolution. At present, evapotranspiration and rainfall are determined with ground-based data and remote sensing technology. Ground-based data supports the temporal resolution, but it is weak for spatial resolution. However, remote sensing observations bolster spatial resolution. Given the differing advantages of the above measurement methods, a combination of ground-based data and remote sensing should be used for the evaluation of evapotranspiration and rainfall to provide more accurate results. In this dissertation, the spatial and temporal variation of evapotranspiration and rainfall for the Chao Phraya River Basin are considered from both ground-based data and remote sensing data. Thereafter, water budgets are computed by using estimated evapotranspiration and rainfall as well as available groundwater data. Finally, the results are applied to water management.

This dissertation is the first of four Engineering Doctoral dissertations directed towards improving the management of the available water supplies in the Chao Phraya River Basin during both the wet season and the dry season. The results from this dissertation research will feed into the third dissertation that utilizes water budgets, rainfall and weather forecasting to predict the daily flows in the river network of the Chao Phraya River Basin.

Regarding the contribution of this dissertation research, the combination of evapotranspiration and rainfall from satellite imagery to compute water balances in

large scale, the Chao Phraya River Basin, is new. Accordingly, after the methodologies for estimation of evapotranspiration using remote sensing technology are learned, then common methods for calculating water budgets that can be applied to river basins and analyzing water management situations may be used. While the results from this research are intended to be useful for Thailand, the methodology can also be applied in other countries around the world.

The purposes of this research are:

1. To analyze the long-term period of meteorological data.
2. To evaluate the spatial variation of evapotranspiration at various times over a year (temporal) for the Chao Phraya River Basin using MODIS images and SEBAL.
3. To determine the crop coefficients for rice, maize, and sugarcane.
4. To calculate the spatial and temporal rainfall using the combination of TRMM image and meteorological data.
5. To compute monthly water budgets for the Chao Phraya River Basin.

The scope of this doctoral research is detailed below.

1. The key component of this research is using remote sensing satellite imagery, in conjunction with appropriate computer hardware and software, to determine the spatial and temporal variability of evapotranspiration and rainfall over the Chao Phraya River Basin.
2. In the remote sensing technology, MODIS imagery is used for calculating evapotranspiration, while rainfall is determined from TRMM imagery. Satellite images will be selected that cover a time period of one year.
3. No hydrologic field data will be collected. Only available hydrologic records will be used.
4. The time duration for the analysis of meteorological data is 1971 to 2002, a 32-year time period.

5. The reliability of evapotranspiration calculated by SEBAL is equal to that computed by the FAO Penman-Monteith method. Also, the reliability of rainfall determined from TRMM images is equal to that from recorded rainfall.

LITERATURE REVIEW

The Chao Phraya River Basin

Description of the Chao Phraya River Basin

In Thailand, the Chao Phraya River Basin is the largest and most important geographical unit in the terms of land and water resources development. It is located in the north and central regions of the country as show in Figure 1. The area of the Chao Praya River Basin is 157,925 km^2. The Chao Phraya River Basin includes eight sub-basins that are Ping, Wang, Yom, Nan, Sakae Krang, Pasak, Tha Chin, and Chao Phraya sub-basins as shown in Figure 2. Large irrigation projects in the Chao Phraya River Basin consist of 44 projects, which are located in 15 provinces; namely Chai Nat, Sing Buri, Ang Thong, Ayutthaya, Lop Buri, Saraburi, Nonthaburi, Pathum Thani, Nakorn Sawan, Suphan Buri, Nakorn Pathom, Samutsakorn, Samutpakarn, Chachoengsao, and Bangkok. Total project irrigated area is 15,717 km^2.

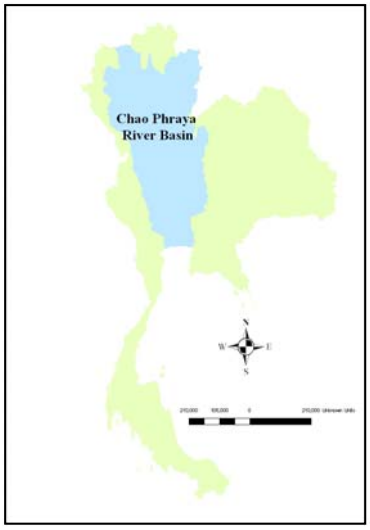

Figure 1 The location of the Chao Phraya River Basin in Thailand

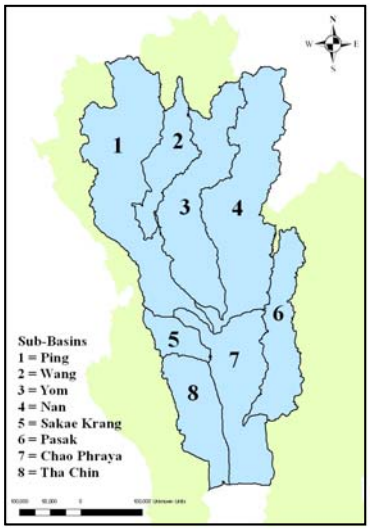

Figure 2 The location of eight sub-basins in the Chao Phraya River basin

The average yearly rainfall is about 1,200 mm in the northern region and 1,350 mm in the Central Valley, where the peak is in September and the dry months are November through April. The rainy season starts from the middle of April and ends in late October. At the beginning stage of the rainy season, it rains locally and within short periods. Non-rain days sometimes continue for quite a long period. The runoff ratio is difficult to calculate. However, it is estimated between 15 and 30% (Buddhapalit, 1999). Tidal effects sometimes come to Ang Thong. This area often suffers from water shortages and flooding. Therefore, good water operations are essential for the prosperity of the area.

The Chao Phraya River Basin drains into the gulf of Thailand, part of the South China Sea and the Pacific Ocean. The headwaters of the Chao Phraya River Basin originate in the mountainous terrain of the northern part of the country and include four large rivers that are the Ping, the Wang, the Yom, and the Nan Rivers. These four upstream rivers flow southward to meet at Nakhon Sawan and form the Chao Phraya River. The Chao Phraya river flows southward through a large alluvial plain or the delta area, splitting into four channels that are the Tha Chin, the Noi, the Lop Buri and the Chao Phraya Rivers.

The river basin can be characterized geographically into the upper and lower basins. The upper basin is mountainous. The main water reservoirs in the basin are the Bhumiphol Reservoir with a storage capacity of 13,500 MCM (million cubic meters) and the Sirikit Reservoir with a storage capacity of 9,500 MCM. Bhumibol Dam and Sirikit Dam are located in the northern sub-basin. These two dams are the largest to supply stored water for irrigation, electricity generation, domestic and industrial water use, and so on. The Pasak Reservoir storage capacity is 960 MCM. The Chao Phraya diversion dam in the Chao Phraya River at Chainat allows water to be allocated for the delta area (Sathianpatarit *et al.*, 2002).

Water Management in Chao Phraya River Basin

The Chao Phraya River Basin is used for agriculture and covered with forest. The major forest areas are in the northern sub-basins, those are Ping, Wang, Yom, and Nan. The Chao Phraya sub-basin also has some forest area. Agricultural areas are concentrated in the southern sub-basins and ranges from 78% in the Chao Phraya, 63% in Pasak and 55% in Tha Chin compared to 20 to 45% in the four northern sub-basins (Ping, Wang, Yom and Nan).

Water availability is a key factor for constraining future agricultural development in the Central Plain, because it is the core of multi-cropping and for crop diversification. Water management for agricultural areas must aim to achieve greater equity and efficiency in water deliveries at the basin, irrigation project, and farm level. For example the achievement of high water use efficiency through crop diversification depends on much greater local level control on water deliveries.

The Royal Irrigation Department (RID) supervises water management in Thailand. Each irrigation project is supervised by RID. Irrigation projects include large-scale, medium, small-scale and pumping projects. In the irrigation project, a zone man is responsible for the distribution of water at the farm level, where cropping patterns and water demands of farmers are recorded. A zone man looks after

approximately 10,000 rai of irrigated area. The zone man will report cropping patterns of farmers in the irrigation project every week. Accordingly, the recording of accurate cropping patterns in all irrigation projects is difficult to achieve.

The Chao Phraya River Basin has 44 large irrigation projects. For the collection of data by RID, the zone man is the first to record and then report to the irrigation project. Thereafter, all irrigation projects report to RID. Due to the large area of the Chao Phraya River Basin, errors occur from this process. At present, satellite imagery is one of many choices to use for recording data in large areas.

Evapotranspiration

In the hydrological cycle and in the water use, evapotranspiration is one of the most important components, but it is one of the most difficult to measure and monitor. Evapotranspiration relates to the exchange of energy in the atmosphere, ground surface, and root zone. Some elements of calculated evapotranspiration can be measured by weather stations, while others are estimated from empirical equations. Then, the calculated evapotranspiration has some inaccuracy. To improve upon this problem, the combination of meteorological data and remote sensing observersions are an alternative evapotranspiration approach (Hongjie, 2002; Hafeez, 2003; Kalluri, 2003).

Evapotranspiration occurs from evaporation and transpiration, and it can be obtained from weather data and satellite images. Evaporation is the primary process of water transfer in the hydrological cycle. The water is transformed into vapour and transported into the sky. Evaporation can be classified into potential evaporation and actual evaporation. The potential evaporation is defined as the amount of evaporation that would occur if a sufficient water source were available. On the other hand, the actual evaporation is the amount of water which is evaporated a normal day. The potential evaporation is the maximum value of the actual evaporation. Transpiration is included by the vaporization of liquid water contained in plant tissues and the vapor removal to the atmosphere (Hongjie, 2002; Hafeez, 2003; Kalluri, 2003).

Evapotranspiration is normally computed from the Penman-Monteith equation using weather data. This equation is affected by principal weather parameters such as radiation, air temperature, humidity and wind speed. These parameters can be measured by weather station data and computed by the equation of FAO irrigation and Drainage Paper No. 56 (Allen *et al.*, 1998). In addition to the Penman-Monteith equation, evapotranspiration can be estimated from satellite images such as NOAA AVHRR, LANDSAT TM, and ASTER images. The methodology of evapotranspiration estimated using satellite imagery is normally the energy balance. The main components of the energy balance equation are sensible heat flux, latent heat flux, soil heat flux, and net radiation. These elements relate with incoming and outgoing radiation in the atmosphere, ground surface, and root zone. They are estimated from remote sensing data and weather data (Wei and Sado, 1994; Amin *et al.*, 1997; Xihua *et al.*, 1997; Andrew *et al.*, 2002; Hutado and Artigao, 2002; Kazama and Sahoo, 2002).

The Surface Energy Balance Algorithm for Land or SEBAL (Bastiaanssen *et al.*, 1998) is an image processing model to calculate evapotranspiration by using satellite imagery and weather data with the concept of energy balance at the land surface, so evapotranspiration for each pixel is calculated. Satellite images that can be used in SEBAL are LANDSAT, NOAA-AVHRR, MODIS, and ASTER. The advantages of SEBAL are easily applicable because of minimal collateral data needed, applicable to various climates because of physical concepts, no need for land use classification, no need to involve data demanding hydrology, and is a suitable method for all visible, near-infrared and thermal radiometers. However, the disadvantages of SEBAL include cloud-free conditions being required and that surface roughness is poorly described, so that SEBAL is only suitable for flat terrain (Timmermans *et al.*, 2001; Allen *et al.*, 2001; Lal *et al.*, 2001; Ines, 2002; Hafeez *et al.*, 2002; Mobin, 2002; Timmermans *et al.*, 2002; Abou El-Magd and Tanton, 2003; Brunner *et al.*, 2003; Jacob *et al.*, 2003).

Principles of Evapotranspiration

Evapotranspiration is a variable of primary interest to many end-users of hydrologic data because it represents a loss of usable water from the hydrologic supply (e.g., agriculture, natural resources, and municipalities (Miller *et al.*, 1995)). Evapotranspiration is highly variable both spatially and temporally. The variability in evapotranspiration occurs from the wide spatial variability of precipitation, hydraulic characteristics of soils, and vegetation types and densities. Evapotranspiration has an impact on plant water stress and generation of connective precipitation patterns. Evapotranspiration is required to close both the water and energy budgets.

Evapotranspiration is the summation of all water leaving the soil and plant surfaces for the air above them and is measured as the equivalent depth of water lost over time, (mm/d), (m/s) or any other such rate measure.

Evapotranspiration for a crop can be calculated from the crop coefficient multiplied by reference evapotranspiration. Crop coefficients can be evaluated from land use maps. Land use maps show the types of crops growing in the study area. The value of the crop coefficient depends on the type and age or growth stage of the crop. Reference evapotranspiration has many equations used for estimation such as the formula of Penman, 1948; Monteith, 1965; Thornthwaite, 1948; Hargreaves, 1985.

The Penman (1948) option for potential evaporation calculation is:

$$E_0 = \left(\frac{\delta}{\delta + V}\right)\left(\frac{h_0 - G}{HV}\right) + \left(\frac{V}{\delta + V}\right) f(V)(e_a - e_d) \qquad (1)$$

where E_o is the potential evapotranspiration in mm, δ is the slope of the saturation vapor pressure curve in $kPaC^{-1}$, V is a psychrometer constant in $kPaC^{-1}$, h_0 is the net radiation in MJm^{-2}, G is the soil heat flux in MJm^{-2}, HV is the latent heat of

vaporization in $MJkg^{-1}$, $f(V)$ is a wind speed function in $mmd^{-1}kPa^{-1}$, e_a is the saturation vapor pressure at mean air temperature in kPa, and e_d is the vapor pressure at mean air temperature in kPa.

The temperature function is utilized so as to estimate the latent heat of vaporization as shown in the following equation:

$$HV = 2.50 - 0.0022T \tag{2}$$

where T is the mean daily air temperature in C. The saturation vapor pressure is also estimated as a function of temperature by using the equation:

$$e_a = 0.1\exp\left(54.88 - 5.03\ln(T+273) - \frac{6791}{T+273}\right) \tag{3}$$

The vapor pressure is simulated as a function of the saturation value and the relative humidity:

$$e_d = (e_a)(RH) \tag{4}$$

where RH is the relative humidity expressed as a fraction. The slope of the saturation vapor pressure curve, δ, is estimated with the equation:

$$\delta = \left(\frac{e_a}{T+273}\right)\left(\frac{6791}{T+273} - 5.03\right) \tag{5}$$

The psychrometer constant is computed with the equation:

$$V = 6.6\times10^{-4} PB \tag{6}$$

where PB is the barometric pressure (kPa).

The barometric pressure is estimated as a function of elevation by using the equation:

$$PB = 101 - 0.0115 ELEV + 5.44 \times 10^{-7} ELEV^2 \quad (7)$$

where ELEV is the elevation of the site in m.

The soil heat flux is estimated by using air temperature on the day of interest plus 3 days prior.

$$G = 0.12\left[T_i - \left(\frac{T_{i-1} + T_{i-2} + T_{i-3}}{3} \right) \right] \quad (8)$$

where T_i is the mean daily air temperature on day i in C where G is usually relatively small.

Solar radiation is adjusted to obtain net radiation by using the equation:

$$h_{oi} = RA_i \left(1.0 - AB_i\right) - RAB_i \left(\frac{0.9 RA_i}{RAMX_i} + 0.1 \right) \quad (9)$$

where RA is the solar radiation in MJm^{-2}, AB is albedo, RAB is the net outgoing long wave radiation in MJm^{-2} for clear days, and RAMX is the maximum solar radiation possible in MJ/m^{-2} for the location on day i.

The RAB value is estimated with the equation:

$$RAB_i = 4.9 \times 10^{-9} \left(0.34 - 0.14\sqrt{e_d}\right)\left(T_i + 273\right)^4 \quad (10)$$

The maximum possible solar radiation is computed with the equations:

$$RAMX = 30\left(1.0 + 0.0335\sin\left[\frac{2\Pi}{365}(i+88.2)\right]\sin\left(\frac{2\Pi}{360}LAT\right)\sin(SD) + \cos\left(\frac{2\Pi}{360}LAT\right)\cos(SD)\sin(XT)\right) \tag{11}$$

$$XT = \cos^{-1}\left(-\tan\left(\frac{2\Pi}{360}LAT\right)\tan(SD)\right), 0 \le XT \le \Pi \tag{12}$$

where LAT is the latitude of the site in degrees, SD is the sun's declination angle (radians), and i is the day of the year.

The sun's declination angle is calculated with the equation:

$$SD_i = 0.4102\sin\left[\frac{2\Pi}{365}(i-80.25)\right] \tag{13}$$

Finally, the wind function of the Penman equation is approximated with the relationship

$$f(V) = 2.7 + 1.63V \tag{14}$$

where V is the mean daily wind speed at a 10-m height in ms^{-1}.

The Penman-Monteith method (Monteith, 1965) was recently added to provide a means for estimating the effects of CO_2 changes (Stockle *et al.*, 1992). The Penman-Monteith equation is expressed as:

$$E_0 = \frac{\delta(h_0 - G) + 86.7AD(e_a - e_d)/AR}{(HV)(\delta + V)} \tag{15}$$

and

$$E_p = \frac{\delta\left(h_0 - G\right) + 86.7\,AD\left(e_a - e_d\right)/\,AR}{HV\left(\delta + V\left(1 + CR/\,AR\right)\right)} \tag{16}$$

where AD is the air density in gm^{-3}, AR is the aerodynamic resistance for heat and vapor transfer in sm^{-1}, and CR is the canopy resistance for vapor transfer in sm^{-1}.

Air density is estimated with the equation:

$$AD = 0.01276PB/\left(1 + 0.0367T\right) \tag{17}$$

The aerodynamic resistance is computed with the equation:

$$AR = \frac{6.25\left(\ln\left(\frac{10 - ZD}{ZO}\right)\right)^2}{V} \tag{18}$$

where ZD is the displacement height of the crop in m, ZO is the surface roughness parameter in m, and V is the daily mean wind speed in ms^{-1}. The surface roughness is estimated with the equation:

$$ZO = 0.131CHT^{0.997} \tag{19}$$

The crop displacement height is estimated with the equation:

$$ZD = 0.702CHT^{0.979} \tag{20}$$

where CHT is crop height in m.

When no crop is growing, the aerodynamic resistance is estimated with the equation:

$$AR = \frac{350}{V} \tag{21}$$

The canopy resistance is computed with the equation:

$$CR = \frac{p_1}{(LAI)(g_o^*)(1.4 - 0.00121CO_2)} \tag{22}$$

where p_1 is a parameter ranging from 1.0 to 2.0, LAI is the leaf-area-index of the crop, g_o^* is the leaf conductance in ms^{-1}, and CO_2 is the carbon dioxide level in the atmosphere in ppm.

Leaf conductance is estimated from the crop input rate adjusted for vapor pressure deficit (VPD):

$$g_o^* = (g_o)(FV) \tag{23}$$

where g_o is the crops leaf resistance when the VPD is less than the crops threshold VPD and FV is the VPD correction factor.

$$FV = 1 - b_V (VPD - VPD_t) \geq 0.1 \tag{24}$$

where b_v is a crop coefficient and VPD_t is a threshold VPD for the crop.

The Priestly-Taylor (1972) method provides estimates of potential evapotranspiration without wind and relative humidity inputs. The simplified equation based only on temperature and radiation is:

$$E_o = 1.28\left(\frac{h_o}{HV}\right)\left(\frac{\delta}{\delta + V}\right) \tag{25}$$

The net radiation is estimated with the equation:

$$h_{oi} = RA_i\left(1 - AB_i\right) \tag{26}$$

The Hargreaves method (Hargreaves and Samani, 1985) estimates potential evaportranspiration as a function of extraterrestrial radiation and air temperature. The Hargreaves method was modified for use in EPIC by increasing the temperature difference exponent from 0.5 to 0.6. Also, extraterrestrial radiation is replaced by $RMAX$ (maximum possible solar radiation at the earth's surface) and the coefficient is adjusted from 0.0023 to 0.0032 for proper conversion. The modified equation is:

$$E_o = 0.0032\left(\frac{RAMX}{HV}\right)\left(T + 17.8\right)\left(T_{\max} - T_{\min}\right)^{0.6} \tag{27}$$

where $T_{\max}$ and $T_{\min}$ are the daily maximum and minimum air temperatures in C.

The albedo for all of the above four methods is estimated by considering the soil, crop, and snow cover. If snow exists with 5 mm or greater of water content, the albedo is set to 0.6. On the other hand, if a snow cover is less than 5 mm and no crop is growing, the soil albedo is the appropriate value. When crops are growing, albedo is determined by using the equation:

$$AB = 0.23\left(1.0 - EA\right) + \left(AB_s\right)\left(EA\right) \tag{28}$$

where 0.23 is the albedo for plants, AB_s is the soil albedo, and EA is a soil cover index. The value of EA ranges from 0 to 1.0 according to the equation:

$$EA = \exp\left(-0.05CV\right) \tag{29}$$

where CV is the sum of the above ground biomass and crop residue in $t*ha^{-1}$.

Reference crop evapotransiration (ET_o) can be calculated on an hourly basis using the FAO Penman-Monteith equation (Allen, 2000):

$$ET_o = \frac{0.408\Delta(R_n - G) + \gamma \frac{900}{T_M + 273.2} u_2 (e_s - e_a)}{\Delta + \gamma(1 + 0.34u_2)} \quad (30)$$

where ET_o is reference crop evapotransiration (mm d^{-1}), R_n is net radiation (MJ $m^{-2}d^{-1}$), G is soil heat flux (MJ $m^{-2}d^{-1}$), T is air temperature (C), e_s is saturation vapor pressure at air temperature (kPa), e_a is vapor pressure of air (kPa), u_2 is wind speed at 2 m (m s^{-1}), Δ is slope of saturation vapor pressure curve at air temperature (kPa C^{-1}), and γ is psychrometer constant (kPa C^{-1}).

For this equation, evapotranspiration is estimated for a hypothetical short grass with a height of 0.12 m, a surface resistance of 70 s m^{-1}, and albedo of 0.23 (Allen *et al.*, 1998; Allen, 2000).

Meteorological factors in order to determine evapotransiration consist of solar radiation, air temperature, air humidity, and wind speed. All of these factors are applied to the FAO Penman-Monteith equation and the following is the process so as to compute elements in this equation.

Atmospheric pressure (P) is defined as the pressure exercised by earth's atmospheric weight. At high altitudes, evaporation is promoted due to low atmospheric pressure as expressed in the psychrometric constant. However, the effect is small and the average value for a location is sufficient for the calculation procedures. A simplification of the ideal gas law, assuming 20 ^{0}C for a standard atmosphere, is obtained to compute P:

$$P = 101.3\left(\frac{293 - 0.0065z}{293}\right)^{5.26} \quad (31)$$

where P is the atmospheric pressure (kPa) and z is elevation above sea level (m).

Latent heat of vaporization (λ) is the energy which is require in order to transfer a unit mass of water from liquid to water vapor in a constant pressure and constant temperature process. The latent heat of vaporization is a function of temperature that can be calculated from the following equation:

$$\lambda = \left(2.501 - 0.00236\left(T_o - 273\right)\right) \times 10^6 \tag{32}$$

where T_o is expressed in absolute temperature K.

The psychrometric constant (γ) is given by:

$$\gamma = \frac{c_p P}{\varepsilon \lambda} \tag{33}$$

where γ is the psychrometric constant (kPa $^0C^{-1}$), c_p is specific heat at constant pressure, 1.013 x 10^{-3} (MJ kg^{-1} $^0C^{-1}$), and ε is the ratio of the molecular weight of water vapor/dry air = 0.622.

In this FAO Penman-Monteith equation, mean daily air temperature (T_{mean}) in ^0C is employed to compute the slope of the saturation vapor pressure curve (Δ) in kPa $^0C^{-1}$ as described below:

$$T_{mean} = \frac{T_{\max} + T_{\min}}{2} \tag{34}$$

$$\Delta = \frac{4098\left[0.6108 \exp\left(\frac{17.27 T_{mean}}{T_{mean} + 237.3}\right)\right]}{\left(T_{mean} + 237.3\right)^2} \tag{35}$$

To obtain the mean saturation vapor pressure (e_s) in kPa, the following are the calculation procedures.

$$e^o(T) = 0.6108 \exp\left[\frac{17.27T}{T + 237.3}\right] \tag{36}$$

where $e^o(T)$ is saturation vapor pressure at the air temperature T (kPa), T is the air temperature (^{0}C), exp function returns **e** (the base of natural logarithms) raised to a power. The return value is the power of the constant **e**. The constant **e** is Euler's constant, approximately equal to 2.178.

Then

$$e_s = \frac{e^o(T_{\max}) + e^o(T_{\min})}{2} \tag{37}$$

The actual vapor pressure (e_a) in kPa can be obtained from relative humidity data as follows:

$$e_a = \frac{e^o(T_{\min})\frac{RH_{\max}}{100} + e^o(T_{\max})\frac{RH_{\min}}{100}}{2} \tag{38}$$

where $e^o(T_{\min})$ is saturation vapor pressure at daily minimum temperature (kPa), $e^o(T_{\max})$ is saturation vapor pressure at daily maximum temperature (kPa), $RH_{\max}$ is maximum relative humidity (%), and $RH_{\min}$ minimum relative humidity (%).

Extraterrestrial radiation (R_a) is calculated for the midday of each month using the following:

$$R_a = \frac{24(60)}{\pi} G_{sc} d_r \left[\omega_s \sin(\varphi)\sin(\delta) + \cos(\varphi)\cos(\delta)\sin(\omega_s)\right] \quad (39)$$

where R_a is extraterrestrial radiation (MJ m^{-2} d^{-1}), G_{SC} = solar constant in MJ m^{-2} d^{-1} = 0.0820 MJ m^{-2} min^{-1} , and the other parameters, such as inverse relative distance Earth-Sun (d_r), sunset hour angle in rad (ω_s), latitude in rad (φ), and solar declination in rad (δ), are obtained from the following equations:

$$d_r = 1 + 0.033\cos\left(\frac{2\pi}{365} J\right) \quad (40)$$

$$\delta = 0.409\sin\left(\frac{2\pi}{365} J - 1.39\right) \quad (41)$$

$$\varphi = \frac{\pi}{180}\left(DecimaiDegrees\right) \quad (42)$$

$$\omega_s = \frac{\pi}{2} - \arctan\left[\frac{-\tan(\varphi)\tan(\delta)}{X^{0.5}}\right] \quad (43)$$

where

$$X = 1 - \left[\tan(\varphi)\right]^2\left[\tan(\delta)\right]^2 \quad (44)$$

and X = 0.00001 if X $\leq$ 0

Daylight hours (N) are given by:

$$N = \frac{24}{\pi}\omega_s \quad (45)$$

Since solar radiation cannot be measured directly, it can be computed from the following equation:

$$R_s = \left(a_s + b_s \frac{n}{N} \right) R_a \tag{46}$$

where R_s is the solar or shortwave radiation (MJ m^{-2} d^{-1}), n is actual duration of sunshine (h), N is maximum possible duration of sunshine or daylight hours (h), n/N is relative sunshine duration (-), and $a_s + b_s$ is the fraction of extraterrestrial radiation reaching the earth on a clear day (n = N) where FAO recomments that a_s and b_s should be 0.25 and 0.50, respectively.

Clear-sky solar radiation, R_{so}, (MJ m^{-2} d^{-1}) is obtained from the equation below:

$$R_{so} = \left(0.75 + 2 \times 10^{-5} z\right) R_a \tag{47}$$

where z is the elevation of a station above sea level (m).

Then, net solar or net shortwave radiation is calculated by:

$$R_{ns} = (1 - \alpha) R_s \tag{48}$$

where R_{ns} is net solar or shortwave radiation (MJ m^{-2} d^{-1}), and α is albedo or canopy reflection coefficient, which is 0.23 for the hypothetical grass reference crop.

To determine net long-wave radiation, the following equation is used:

$$R_{nl} = \sigma \left[\frac{T_{\max,K^4} + T_{\min,K^4}}{2} \right] \left(0.34 - 0.14\sqrt{e_a}\right) \left[1.35 \frac{R_s}{R_{so}} - 0.35 \right] \tag{49}$$

where R_{nl} is net outgoing long-wave radiation (MJ m^{-2} d^{-1}), σ is the Steffan-Boltzman constant = 4.90 x 10^{-9} (MJ m^{-2} $d^{-1}K^{-4}$), $T_{\max,K^4}$ is maximum absolute temperature during the 24-hour period $\left[K = {}^0C + 273.16\right]$, $T_{\min.K^4}$ is minimun absolute temperature during the 24-hour period $\left[K = {}^0C + 273.16\right]$ and $\frac{R_s}{R_{so}}$ is relative shortwave radiation (limited to $\leq$ 1.0).

Then, the difference between the incoming net shortwave radiation and the outgoing net long-wave radiation is the net radiation (R_n) as shown by the following equation:

$$R_n = R_{ns} - R_{nl} \tag{50}$$

The soil heat flux (G) can be described by a complex model, but soil heat flux is small compared to R_n. Thus, the soil heat flux can be computed from the following equation which is based on the idea that the soil temperature follows air temperature:

$$G = c_s \frac{T_i - T_{i-1}}{\Delta t} \Delta z \tag{51}$$

where G is soil heat flux (MJ m^{-2} d^{-1}); c_s is soil heat capacity (MJ m^{-3} $^0C^{-1}$); T_i is air temperature at time i (^{0}C); T_{i-1} is air temperature at time i-1 (^{0}C); Δt is length of time interval (day); and Δz is effective soil depth (m).

FAO recommends that as the magnitude of the day or ten-day soil heat flux beneath the grass reference surface is relatively small, it may be ignored and thus:

$$G_{day} = 0 \tag{52}$$

Radiation

Extraterrestrial (solar) radiation (R_a) is the solar radiation received at the top of the earth's atmosphere on a horizontal surface. The values of extraterrestrial radiation depend on seasons change, position of the sun, and length of the day. Therefore, the extraterrestrial radiation is a function of latitude, date and time of day. The solar constant is the radiation striking a surface perpendicular to the sun's rays at the top of the earth's atmosphere, and it is some 0.082 MJ m^{-2} min^{-1}. If the position of the sun is directly overhead, the incidence angle of extraterrestrial radiation is zero. In this case, extraterrestrial radiation is some 0.082 MJ m^{-2} min^{-1}.

Solar or shortwave radiation (R_s) is the amount of radiation penetrating from the atmosphere to a horizontal plane. The sun emits energy by electromagnetic waves that have short wavelengths, so solar radiation is referred to as shortwave radiation. In the atmosphere, radiation is absorbed, scattered, or reflected by gases, clouds, and dust. For a cloudless day, solar radiation is about 75% of the extraterrestrial radiation, while solar radiation is about 25% of extraterrestrial radiation on a cloudy day. Solar radiation, which is known as global radiation, is a summation of direct shortwave radiation from the sun and diffuse sky radiation from all upward angles.

Relative shortwave radiation (R_s / R_{so}) is a relationship between shortwave radiation (R_s) and clear-sky solar radiation (R_{so}). The shortwave radiation is solar radiation that actually reaches to the earth's surface in a given time, while clear-sky solar radiation is solar radiation that reaches to the same area with a clear-sky condition. The relative shortwave radiation is affected by the cloudiness of the atmosphere. On a cloudy day, the ratio is smaller than on a cloudless day. The range of this ratio is between 0.33 (cloudy condition) to 1.00 (cloudless condition).

Relative sunshine duration (n/N) shows the cloudiness in the atmosphere. It is the relationship between actual duration of sunshine (n) and maximum possible duration of sunshine, or daylight hours (N). For the cloudless condition, n is equal to

N, while n and n/N are nearly zero for the cloudy condition. The maximum possible duration of sunshine, or daylight hours (N), depends on the position of the sun, so it is a function of latitude and date. The daily values of N throughout a year differ with latitude.

Albedo (α) is a relationship between reflected radiation and total incoming radiation. It varies with the characteristics of the surface and angle of incidence, or the slope of the ground surface. Albedo can be more than 0.95 for freshly fallen snow, and it is smaller than 0.05 for wet bare soil. The range of albedo for green vegetation is about 0.20 – 0.25 and albedo for the green grass reference crop is 0.23.

Net solar radiation (R_{ns}) is the fraction of the solar radiation that is reflected from the ground surface. It can be calculated by Equation (53):

$$R_{ns} = (1-\alpha)R_s \tag{53}$$

Net longwave radiation (R_{nl}) is the difference in value between outgoing and incoming longwave radiation. The longwave radiation is that solar radiation absorbed by the earth and turned to heat energy. Since the temperature of the earth is less than the sun, so the earth emits longer wavelengths. Terrestrial radiation is referred to as longwave radiation. The emitted longwave radiation ($R_{l,up}$) is absorbed by the atmosphere, or lost into space. The longwave radiation received by the atmosphere ($R_{l,down}$) increases its temperature. Therefore, the earth's surface both emits and receives longwave radiation. The value of outgoing longwave radiation is normally more than incoming longwave radiation, so net longwave radiation is used to present the energy loss.

Net radiation (R_n) is the difference in value between incoming and outgoing radiation of both short and long wavelengths. It is the balance between energy absorbed, reflected, and emitted by the earth's surface. The net radiation is also the

difference in value between the incoming net shortwave (R_{ns}) and the net outgoing longwave (R_{nl}) radiation. It is a positive value during daytime, while it is a negative value during nighttime. For the total daily value, it is a positive value except for the condition of high latitude.

Soil heat flux (G) is energy that is used in heating the soil. It is a positive value under the condition of warming soil, and negative under the condition of cooling soil. The soil heat flux is very small when compares with net radiation, but it cannot be ignored.

Principle of SEBAL

SEBAL is used to calculate evapotranspiration with satellite images and weather data by using the concept of energy balance at the land surface. SEBAL needs both shortwave and thermal bands. The required ground-based data is wind speed. The SEBAL energy balance calculates evapotranspiration for each pixel for the time of the satellite image, so the results are instantaneous evapotranspiration (Bastiaanssen *et al.*, 1998; Bastiaanssen, 2000; Chemin and Ahmad, 2000; Allen and Bastiaanssen, 2002; Bastiaanssen *et al.*, 2002). The principal elements of SEBAL are reflectance of light energy, vegetation indices, surface temperature, relative variation in surface temperature, and general wind speed. The main equation of SEBAL is shown as follows:

$$LE = (R_n - G) - H \tag{54}$$

where LE is the latent energy of evaporation (W/m^2), R_n is the net radiation flux at the soil surface (W/m^2), G is the soil heat flux (W/m^2), and H is the sensible heat flux to the air (W/m^2).

Net radiation flux is input energy into the land surface. It can be calculated from incoming shortwave radiation, incoming and outgoing longwave radiation, surface albedo, and surface thermal emissivity as follows:

$$R_n = R_{s\downarrow} - \alpha R_{s\downarrow} + R_{L\downarrow} - R_{L\uparrow} - (1-\varepsilon_o)R_{L\downarrow} \tag{55}$$

where $R_{s\downarrow}$ is the incoming shortwave radiation (W/m^2), α is the surface albedo (dimensionless), $R_{L\downarrow}$ is the incoming longwave radiation (W/m^2), $R_{L\uparrow}$ is outgoing longwave radiation (W/m^2), and ε_o is the surface thermal emissivity (dimensionless).

Soil heat flux is calculated as a variable fraction of net radiation. It is calculated from Normalize Difference Vegetation Index (NDVI), surface temperature, and surface albedo using the following equation:

$$\frac{G}{R_n} = \frac{T_s}{\alpha}\left(0.0038\alpha + 0.0074\alpha^2\right)\left(1 - 0.98NDVI^4\right) \tag{56}$$

where T_s is surface temperature (^{0}C).

Sensible heat flux to the air is calculated by using wind speed observations, estimated surface roughness, and surface to air temperature differences in the following equation:

$$H = \frac{\rho \times c_p \times dT}{r_{ah}} \tag{57}$$

where ρ is air density (kg/m^3), c_p is air specific heat (1004 J/kg/K), dT (K) is the temperature difference (T_1-T_2) between two heights (z_1 and z_2), and r_{ah} is the aerodynamic resistance to heat transport (s/m).

The estimation of sensible heat flux is the largest drawback, because dT and r_{ah} are unknown for the sensible heat flux calculation. To find these unknowns, SEBAL first calculates the sensible heat flux at extreme dry and wet locations. They are manually identified by the user on the image. The aerodynamic resistance to heat transport (r_{ah}) is computed from the lower integration constant for r_{ah} (Z_1 = 0.1 m.) and the upper integration constant for r_{ah} (Z_2 = 2 m.).

For a dry pixel or hot pixel, it should be located in a dry and bare agricultural field where one can assume that there is no evapotranspiration taking place. The wet pixel or cold pixel will have a surface temperature equal to air temperature. The sensible heat flux for the cold pixel is usually zero. The linear relationship between dT and T_s ($dT = a + bT_s$) is created, and the coefficients a and b are defined from the two (dT, T_s) pairs applicable to the hot and cold pixels. Then sensible heat flux can be computed for every pixel that has the condition of free convection. Next, the values of friction velocity (u^*) are estimated from the wind speed at the blending height, a value of 200 m will be used. Thereafter, the condition of mixed convection is applied, and the pixel-dependent aerodynamic resistance to heat transfer r_{ah} is calculated by using the Monin-Obukhov hypothesis. The new dT is calculated. Finally the processes from the calculation of sensible heat flux to the temperature difference dT are repeated until the aerodynamic resistance to heat transfer r_{ah} and temperature difference dT are stable values.

After LE is computed, the Evaporative Fraction (Λ) is the next value that is obtained using Equation 58. The Evaporative Fraction at each pixel of a satellite image can be estimated using the 24-hour evaporatranspiration for the day of the image. The evaporative fraction is assumed to be a constant value over the full 24-hour period.

$$\Lambda = \frac{LE}{R_n - G} = \frac{LE}{LE + H} \tag{58}$$

To estimate 24-hour actual evaporatranspiration, the following equation is utilized.

$$ET_{24} = \frac{86400\Lambda\left(R_{n24} - G_{24}\right)}{\lambda} \tag{59}$$

where R_{n24} is daily net radiation, G_{24} is daily soil heat flux, 86,400 is the number of seconds in a 24-hour period, and λ is the latent heat of vaporization (J/kg). The 24-hour actual evaporatranspiration, ET_{24}, can be expressed in mm/day.

Since energy, on average, is stored in the soil during the daytime and released into the air at night, G_{24} is very small for the combined vegetative and soil surface, so it can be assumed as zero at the soil surface (Morse *et al.*, 2000; Hafeez and Chemin, 2002). Then, Equation 59 can be rewritten as:

$$ET_{24} = \frac{86400\Lambda R_{n24}}{\lambda} \tag{60}$$

Satellite Sensors

Satellite images that can be used in SEBAL are LANDSAT, NOAA-AVHRR, MODIS, and ASTER. The characteristic of these satellite sensors are presented below.

LANDSAT

The series of Landsat consist of Landsat 1, Landsat 2, Landsat 3, Landsat 4, Landsat 5, Landsat 6, and Landsat 7. Landsat 7 is the latest in a series of Landsat earth observation satellites. It has a unique and necessary role in the realm of earth observing satellite orbits, because no other satellite of the earth observing system matches with the synoptic coverage, high spatial resolution, spectral range and radiometric calibration of Landsat's system.

The sensors of Landsat 1, Landsat 2, and Landsat 3 are Muti-Spectral Scanner (MSS). Landsat 4 and Landsat 5 used both MSS and TM (Thematic Mapper) sensor, while Landsat 6 consists of both MSS and ETM+ (Enhanced Thematic Mapper Plus). Landsat 7 contains the ETM+ sensor that consists of new features. These features of ETM+ support a more versatile and efficient instrument for global change studies, land cover monitoring and assessment and large area mapping. The details of Landsat 7 and ETM+ characteristic are shown in Table 1 and Table 2.

The ETM+ scanner includes two focal planes that collects, filters, and detects the scene radiation in a swath. The first focal planes contain the filters, detectors, and preamplifiers for bands 1-4 and band 8. The second focal planes or cold focal planes consist of the optical filters, infrared detectors, and input stages for ETM+ spectral bands 5-7. After the ETM+ scanner records and stores data, real-time data from this sensor will be transmitted to cooperating international ground stations and to the U.S. ground stations.

Table 1 Landsat 7 mission specification

Characteristic	Specification
Swath width:	185 km
Repeat coverage interval:	16 days (233 orbits)
Altitude:	705 km
Quantization:	Best 8 of 9 bits
On-board data storage:	~ 375 Gb (solid state)
Inclination:	Sun-synchronous, 98.2 degrees
Equatorial crossing:	Descending node; 10:00 am +/- 15 min
Launch vehicle:	Delta ll
Launch date:	April 1999

Source: Australian Government Geoscience Australia (2004)

At the ground stations, the Landsat ground system consists of a spacecraft control center, ground stations for uplinking commands and receiving data, a data handling facility and a data archive, which were developed by the Goddard Space Flight Center, Greenbelt, MD., in conjunction with the U.S. Geological Survey (USGS) EROS Data Center (EDC), Sioux Falls, SD. These facilities will receive, process, archive, and distribute ETM+ data to users. Raw ETM+ data can be transmitted to the EROS Data Center by the ground system within 24 hours of its reception (Farr, 1999; Liu, 2000; and Liang, 2001).

Table 2 Landsat 7 and ETM+ characteristic

Channel	Spectral Range (microns)	Ground Resolution (m)
1 (Visible and near infrared: VNIR)	0.450 - 0.515	30
2 (Visible and near infrared: VNIR)	0.525 - 0.605	30
3 (Visible and near infrared: VNIR)	0.630 - 0.690	30
4 (Visible and near infrared: VNIR)	0.750 - 0.90	30
5 (Short wavelength infrared: SWIR)	1.550 - 1.750	30
6 (Thermal long wavelength infrared: LWIR)	10.40 - 12.50	60
7 (Short wavelength infrared: SWIR)	2.090 - 2.350	30
Pan (Visible and near infrared: VNIR)	0.520 - 0.900	15

Source: Farr (1999)

NOAA-AVHRR

The series of NOAA includes TIROS-N, NOAA-6, NOAA-7, NOAA-8, NOAA-9, NOAA-10, NOAA-11, NOAA-12, NOAA-13, and NOAA-14. For all of these NOAA satellites, only the NOAA-14 is used presently. The satellite orbits the Earth 14 times each day from 833 km above its surface. Each pass of the satellite is a 2,399 km wide swath. For the NOAA satellite system, there are two instrument packages; TOVS (TIROS Operational Vertical Sounder) and AVHRR (Advanced

Very High Resolution Radiometer). The TOVS includes a Microwave Sounding Unit (MSU), a Stratospheric Sounding Unit (SSU), and a High Resolution Infrared Radiation Sounder/2 (HIRS/2), while the AVHRR consists of High Resolution Direct Readout AVHRR (HRPT), Local Area Coverage (LAC), and Global Area Coverage (GAC).

The AVHRR is a broad-band sensor in the visible, near-infrared, and thermal infrared portions of the electromagnetic spectrum. The AVHRR sensor provides global (pole to pole) on-board collection of data from all of these spectrum channels. The significant functions of this sensor consists of:

- deriving Sea Surface Temperatures (operational NOAA product);
- deriving the Normalized Difference Vegetation Index or NDVI (operational NOAA product);
- deriving atmospheric aerosols over the oceans (operational NOAA product);,
- monitoring volcanic eruptions and supporting an operational NOAA warning of volcanic ash in the atmosphere during eruption events; and
- other applications requiring the high temporal resolution of global daily coverage, with spatial resolution and moderate spectral, operational side-lap stereoscopic coverage, and calibrated thermal sensors.

According to the above advantages, the AVHRR can be used to produce various operational data sets. Also, AVHRR data help prepare opportunities for studying and monitoring vegetation conditions in ecosystems, which includes forests, tundra, and grasslands. Application and related data sets of AVHRR consists of agricultural assessment, land cover mapping, producing image maps of large areas (such as countries or continents) and tracking regional and continental snow cover (NCDC, 1998; NASA, 2002; NGDC, 2003).

MODIS

MODIS or Moderate Resolution Imaging Spectroradiometer is a primary instrument for terrestrial observation on the Earth Observing System (EOS). The MODIS instrument consists of a ± 55 degree scanning pattern at the EOS orbit of 705 km that achieves a 2,330 km swath. Key instruments aboard the MODIS include the Terra (EOS AM) and Aqua (EOS PM) satellites. The Terra passes from north to south across the equator in the morning, while the Aqua passes from south to north over the equator in the afternoon. Both the Terra MODIS and the Aqua MODIS are viewing the entire Earth's surface every 1 to 2 days, which acquires data in 36 spectral, or groups of wavelength bands, which ranges from 0.4 μm to 14.4 μm, as shown in Table 3. These data are provided for the understanding of global dynamics and processes occurring on the land, in the oceans, and in the lower atmosphere.

The MODIS data product consists of 44 standard products that are used for the study of global change. Table 4 shows the standard MODIS data products. These products are used by scientists from a variety of disciplines, including oceanography, biology, and atmospheric science (Borak, 1999; Gutman, 2002; Conboy, 2003; IODE, 2003).

ASTER

ASTER (or the Advanced Spaceborne Thermal Emission and Reflection Radiometer) is an advanced multispectral imager that is flying on the Terra. The ASTER includes three different subsystems as shown in Table 5; visible and near infrared (VNIR), shortwave infrared (SWIR), and thermal infrared (TIR). The VNIR consists of three bands with a spatial resolution of 15 m, and an additional backward telescope for stereo. The SWIR has six bands with a spatioal resolution of 30 m. The TIR includes five bands with a spatial resolution of 90 m. The advantage of ASTER is to obtain detailed maps of land surface temperature, emissivity, reflectance and elevation (Abrams *et al.*, 2003; NASA, 2003).

Table 3 The MODIS spectral bands

Primary Use	Band	Bandwidth		Spectral Radiance W/m^2 - μm -sr	
Land/Cloud/Aerosols	1	620-670	nm	21.8	
Boundaries	2	841-876	nm	24.7	
Land/Cloud/Aerosols	3	459-479	nm	35.3	
Properties	4	545-565	nm	29.0	
	5	1230-1250	nm	5.4	
	6	1628-1652	nm	7.3	
	7	2105-2155	nm	1.0	
Ocean Color/Phytoplankton/	8	405-420	nm	44.9	
Biogeochemistry	9	438-448	nm	41.9	
	10	483-493	nm	32.1	
	11	526-536	nm	27.9	
	12	546-556	nm	21.0	
	13	662-672	nm	9.5	
	14	673-683	nm	8.7	
	15	743-753	nm	10.2	
	16	862-877	nm	6.2	
Atmospheric Water Vapor	17	890-920	nm	10.0	
	18	931-941	nm	3.6	
	19	915-965	nm	15.0	
Surface/Cloud/Temperature	20	3.660-3.840	μm	0.45	(300K)
	21	3.929-3.989	μm	2.38	(335K)
	22	3.929-3.989	μm	0.67	(300K)
	23	4.020-4.080	μm	0.79	(300K)

Table 3 (cont'd)

Primary Use	Band	Bandwidth	Spectral Radiance W/m2 - μ m -sr
Atmospheric Temperature	24	4.433-4.498 μ m	0.17 (250K)
	25	4.482-4.549 μ m	0.59 (275K)
Cirrus Clouds Water Vapor	26	1.360-1.390 μ m	6.00
	27	6.535-6.895 μ m	1.16 (240K)
	28	7.175-7.475 μ m	2.18 (250K)
Cloud Properties	29	8.400-8.700 μ m	9.58 (300K)
Ozone	30	9.580-9.880 μ m	3.69 (250K)
Surface/Cloud Temperature	31	10.780-11.280 μ m	9.55 (300K)
	32	11.770-12.270 μ m	8.94 (300K)
Cloud Top Altitude	33	13.185-13.485 μ m	4.52 (260K)
	34	13.485-13.785 μ m	3.76 (250K)
	35	13.785-14.085 μ m	3.11 (240K)
	36	14.085-14.385 μ m	2.08 (220K)

Source: Conboy (2003)

Table 4 The 44 standard MODIS data products

Data Type	Description
Calibration	MOD 01 - Level-1A Radiance Counts
	MOD 02 - Level-1B Calibrated Geolocated Radiances
	MOD 03 - Geolocation Data Set
Atmosphere	MOD 04 - Aerosol Product
	MOD 05 - Total Precipitable Water (Water Vapor)
	MOD 06 - Cloud Product
	MOD 07 - Atmospheric Profiles
	MOD 08 - Gridded Atmospheric Product
	MOD 35 - Cloud Mask
Land	MOD 09 - Surface Reflectance
	MOD 11 - Land Surface Temperature & Emissivity
	MOD 12 - Land Cover/Land Cover Change
	MOD 13 - Gridded Vegetation Indices (Max NDVI & Integrated MVI)
	MOD 14 - Thermail Anomalies, Fires & Biomass Burning
	MOD 15 - Leaf Area Index & FPAR
	MOD 16 - Evapotranspiration
	MOD 17 - Net Photosynthesis and Primary Productivity
	MOD 43 - Surface Reflectance
	MOD 44 - Vegetation Cover Conversion
Cryosphere	MOD 10 - Snow Cover
	MOD 29 - Sea Ice Cover

Table 4 (cont'd)

Data Type	Description
Ocean	MOD 18 - Normalized Water-leaving Radiance
	MOD 19 - Pigment Concentration
	MOD 20 - Chlorophyll Fluorescence
	MOD 21 - Chlorophyll_a Pigment Concentration
	MOD 22 - Photosynthetically Available Radiation (PAR)
	MOD 23 - Suspended-Solids Concentration
	MOD 24 - Organic Matter Concentration
	MOD 25 - Coccolith Concentration
	MOD 26 - Ocean Water Attenuation Coefficient
	MOD 27 - Ocean Primary Productivity
	MOD 28 - Sea Surface Temperature
	MOD 31 - Phycoerythrin Concentration
	MOD 36 - Total Absorption Coefficient
	MOD 37 - Ocean Aerosol Properties
	MOD 39 - Clear Water Epsilon

Source: Conboy (2003)

The Experience of SEBAL Calculations with Satellite Images

For the SEBAL method, Landsat was the first satellite image to be used for this method, and NOAA, MODIS, and ASTER satellite images were later used. The experiences in calculating evapotranspiration with SEBAL using satellite images are presented below.

In 1994, Wei and Sado reported a study under the title "Estimation of Areal Evapotranspiration Using Landsat TM Data Alone" to investigate the possibility of using the Landsat TM 7 bands data alone to estimate evapotranspiration over large areas. Study areas for this research were Tokoro River Basin and Abashiri River Basin in Japan. Various regression analyses were conducted. The relationship between these data from Landsat and the real evapotranspiration or potential evapotranspiration from the Penman equation was established. The results showed that the effective estimation of evapotranspiration for grassland, forest, water, and paddy fields by using only the Landsat TM data only was suitable.

In 2000, Kite and Droogers studied under the title "Comparing evapotranspiration estimates from satellites, hydrological model, and field data" to provide an overview of an experiment in which eight different methods were used for estimating actual evaporation and transpiration based on field data. These eight methods are: (1) FAO-24; (2) FAO-56; (3) large aperture scintillometer; (4) SWAP; (5) SLURP; (6) satellite-derived feedback mechanism; (7) biophysical processes with remotely sensed data; and (8) SEBAL remote sensing technique. The results showed that the methods of (1), (6), (7), and (8) have the greatest variability. The methods of (2), (3), (4), and (5) show more consistency. For SEBAL calculations with NOAA-AVHRR and Landsat TM, the research presents that high spatial resolution (especially for the Landsat TM) and high spatial coverage (especially for the NOAA-AVHRR) are an advantage, while the disadvantage of SEBAL is that only instantaneous estimates can be obtained.

Table 5 The spectral band passes of ASTER Satellite Sensors

Subsystem	Band No.	Spectral Range (μm)	Spatial Resolution, m.	Quantization Level
VNIR	1	0.520-0.600	15	8 bits
	2	0.630-0.690		
	3N	0.780-0.860		
	3B	0.780-0.860		
SWIR	4	1.600-1.700	30	8 bits
	5	2.145-2.185		
	6	2.185-2.225		
	7	2.235-2.285		
	8	2.295-2.365		
	9	2.360-2.430		
TIR	10	8.125-8.475	90	12 bits
	11	8.475-8.825		
	12	8.925-9.275		
	13	10.25-10.95		
	14	10.95-11.65		

Source: NASA (2003)

In 2001, Timmermans *et al.* presented the results of a study under the title "Satellite derived actual evapotranspiration and groundwater modeling, Botswana" to determine evapotranspiration losses over an aquifer during a dry season in Botswana with the SEBAL, using sequential Landsat TM and NOAA-AVHRR data, with concurrent meteorological field data for atmospheric correction and calibration. The SEBAL method yielded high actual evapotranspiration rates (<0.5 to 4 mm per day) if the relatively dense savanna vegetation was present, even when ground water was over 40 m deep.

In 2002, Hafeez *et al.* presented their study having the title "Field Evapotranspiration Estimation in Central Luzon, Philippines, Using Different Sensors: Landsat 7 ETM+, Terra MODIS and ASTER". The SEBAL has been applied to these three satellite images to estimate evapotranspiration in the District 1 of the Upper Pumapanga River Integrated Irrigation System in Central Luzon of the Philippines. The actual evapotranspiration was calculated during satellite overpasses and integrated for 24-hours on a pixel-by-pixel basis. This research presented a unique combination and inter-relationship of the ASTER, and the Landsat images with the MODIS images for the water consumption studies in District 1. The results were compared with the evapotranspiration calculation at two meteorological stations in this study area. This comparison found a close relationship with daily evapotranspiration estimated by different sensors as predicted by SEBAL. This research concluded that the results from all three remote sensing platforms can be used for the computation of actual evapotranspiration studies in a tropical climate, but with necessary precautions.

Ahmad (2002) studied "Estimation of net groundwater use in irrigated river basins using geo-information techniques: A case study in Rechna Doab, Pakistan" to develop a methodology for computing the various water balance components of the unsaturated zone by using geo-information techniques. The components of these water balances were used for the computation of net groundwater use. The SEBAL was used for the calculation of regional scale actual evapotranspiration and soil moisture map, which are two of all components, and SWAP is used to compute sub-soil water fluxes, including recharge and capillary rise. New geomatic approaches were developed and tested that estimate the disaggregated canal water distribution in an irrigation basin, using discharge measurements at main canal offtakes and satellite imagery. The resolution of 30 m for Landsat images produced the highest accuracy of the computed canal water distribution, because Landsat images can be used to identify the shape of the irrigated area. Thus, it can be concluded that high resolution satellite images can be used to discern canal water use from groundwater use.

Ines (2002) studied under the title "Improved crop production integrating GIS and Genetic Algorithm (GA)" to develop a methodology that can be used to explore improved water management options in irrigated agriculture. This was achieved by developing a deterministic-stochastic agro-hydrological model that can simulate regional hydrological processes and crop growth. The quasi-regional model was found to be robust and can define the real water balance and crop growth at every stage of the growing season. A part of the methodology was to develop a system characteristic method by means of a regional inverse modeling. GA was integrated with the regional model for searching of a solution during the inverse modeling. The spatial and temporal distributions of evapotranspiration were considered as fitting criteria in the search. The results of evapotranspiration distribution from the simulation, using the generated parameters from GA as input data, were matched with the measured evapotranspiration in the process. The SEBAL was used to calculate spatial distribution of evapotranspiration using two Landsat 7 ETM+ data on February 4 and March 8, 2001.

Kramber (2002) studied under the title of "Developing Evapotranspiration Data for Idaho's Treasure Valley using the Surface Energy Balance Algorithm for Land (SEBAL)". The SEBAL was applied to 14 Landsat images from 7 dates throughout the 2000 growing season. Seven 24-hour evapotranspiration images and a season evapotranspiration image were the results. The hydrological modeling and regional planning will be created from the season evapotranspiration data.

Muthuwatta (2002) presented the results of a study under the title "Vegetation growth zones using NOAA-AVHRR data: Comparison between conventional and satellite based methods". This study provides an example of using free public satellite data for agricultural planning. The actual biological activities on the ground, which are considered as major factors in demarcating land areas into different zones, is the major innovation of this study. The SEBAL is used to calculate the actual evapotranspiration and evaporative fraction using NOAA-AVHRR images. In addition to that, indicators such as vegetation growth, soil moisture, potential evapotranspiration, and surface temperature were derived. The results showed that

even though the spatial resolution of NOAA-AVHRR is low, it is useful for macro level analysis such as demarcating a country into vegetation growth zones.

Bastiaanssen *et al.* (2002) reported a study under the title of "Satellite surveillance of evaporative depletion across the Indus Basin". This study uses the SEBAL to calculate actual evapotranspiration for a very large area based on the NOAA satellite data for the Indus Basin, because this area has insufficient water resources to supply all of its stakeholders. The estimated evapotranspirations were validated by comparing results from a field-scale transient moisture flow model, in situ Bowen ratio measurement, and residual water balance analyses for an area of 3 million ha. According to the results from this research, spatiotemporal information on actual evapotranspiration helps to estimate water distribution and water use between large irrigation areas. Satellite-based measurements can prepare information and avoid the need to rely on field databases.

In 2003, Brunner *et al.* reported a study under the title "Assessing the groundwater budget for water supply in an area of low groundwater recharge in northern Botswana". The methodological advance of the work includes combining the remote sensing data, the climate data, and the chloride method into a method allowing the calculation of a recharge map for the project area. The groundwater balance was assessed using a combination of techniques based on scarce available data. The SEBAL was used to estimate daily evapotranspiration using NOAA-14 AVHRR. The Penman-Monteith equation was used for the determination of annual variation. Combinations of the yearly evapotranspiration with rainfall data under the assumption of negligible surface runoff were used to define zones of different recharge. The values of the recharge rates were calibrated with recharge values obtained from the chloride mass balance method in specific locations.

Schuurmans *et al.* (2003) studied "Assimilation of remote sensed latent heat flux in a distributed hydrological model" to improve the distribution of hydrological model water balance computations by the process of data assimilation. The SEBAL was used to compute latent heat flux using NOAA-AVHRR satellite data. The

physically-based distributed model SIMGRO (SIMulation of GROundwater flow and surface water level) was used for the calculation of water balances in the same areas and same years. The results of model-derived and remote-sensed area-averaged evapotranspiration estimation showed good agreement after comparison. However, spatial analyses of the model latent heat flux estimates indicate systematic underestimation in areas with higher elevation.

Chandrapala and Wimalasuriya (2003) studied "Satellite measurements supplemented with meteorological data to operationally estimate evaporation in Sri Lanka" to calculate actual evaporation by using the method of SEBAL and the NOAA-AVHRR images in Sri Lanka during the period from June 1999 to 2000. Ground data, including average air temperature and wind speed from the meteorological stations at satellite overpass time and averaged sunshine duration data, were used along with the satellite data. The evaporations, which were estimated from SEBAL, were compared with data from a large aperture scintillometer, that resulted in errors amounting to 17 and 1% in the case of 10-day and monthly evaporation, respectively.

Allen *et al.* (2003) studied "Evapotranspiration from Landsat (SEBAL) for Water Rights Management and Compliance with Multi-State Water Compacts". This study used SEBAL and Landsat images for evapotranspiration calculations in the Bear River Basin of southeastern Idaho, USA. Evapotranspiration for periods in between satellite overpasses was obtained from the ratio between evapotranspiration from SEBAL and reference evapotranspiration which are calculated from ground-based weather stations. These ratios were essentially customized crop coefficients that were determined uniquely for each pixel of an image. The results of this research were used to predict total, net depletion of water from the Bear River system resulting from irrigation diversions.

According to the above SEBAL experiences, SEBAL is normally used for calculation of evapotranspiration using Landsat, NOAA-AVHRR, MODIS, and ASTER satellite images for application to the field of water management. Many

researchers used a number of satellite sensors for comparing the capacity of these satellite sensors. The capacity of each satellite sensor depends on the spatial resolution, where Landsat includes high spatial resolution, while the other satellite sensors consist of lower spatial resolutions than Landsat. For calibration of the results from SEBAL, ground-based data from meteorological stations were used to validate the results from SEBAL.

Rainfall

The estimation of rainfall is complicated by both temporal and spatial variability and brings uncertainty to hydrologic analysis and the calculation of water balances. Temporal variability is caused by the climatic factors governing rainfall: solar radiation, wind, atmospheric humidity, land and sea surface temperatures, and global circulation patterns. Ordinary spatial variability is because of (a) landscape topography and (b) the climatic variables listed above (Sivapalan, 2003). These climatic parameters (including rainfall) can be recorded by meteorological stations on the ground and by various forms of remote sensing from satellites.

Average daily rainfall is estimated using rain gauges. Ideally, any study area would have an adequate density and distribution of rain gauges, but this is rare in many parts of the world. Spatially averaged rainfall over a well-gauged area can be estimated using spatial interpolation techniques. Interpolation techniques can allow the estimation of rainfall in an un-gauged area, which is surrounded by sufficiently well-sited rainfall stations but, due to insufficient density and distribution of rain gauges, the estimation of average rainfall is often in error (Chaubey, 1999).

Rainfall measurement is a basic requirement for calculating the volumes of infiltration and runoff and for the derivation of water balances. Rainfall can be measured by both rain gauges and increasingly by remote sensing techniques. Rain gauges have good temporal resolution, but have poor spatial resolution. However, remote sensing technology has good spatial resolution and relatively poor temporal

resolution compared to tipping bucket rain gauges that may sample over periods of less than two minutes during intense rainfall.

As far as possible, rain gauges are sited in representative locations, although it is common to find significant variation even over a separation distance of a few kilometers (CCFFWS, 2003). There are three main types of rain gauges; non-recording gauges, weighing gauges, and tipping bucket gauges. Non-recording gauges include a small graduated wedge or cylinder that is placed at some height above the ground. These gauges must be read manually once or twice per day. A weighing gauge has a collection bucket, and the depth of water is estimated from the weight in the bucket. Then, rainfall is calculated from the change of water depth. A tipping bucket gauge consists of a funnel and a tipping bucket that is calibrated so that a number of tips correspond to 1 mm of rainfall (typically 4 – 10). This gauge estimates rainfall by using the number of tips in a given period of time and is usually equipped with a built in data logger (Kuligowski, 1996).

Rainfall can be estimated from conventional multi-spectral satellite platforms and from microwave radiation using either radiometers measuring up-welling (passive) microwave radiation, or active radar. Visible and infrared channels are used to estimate rainfall through relationships to cloud temperature. Various sensors are discussed later in this chapter.

Ground-based radar has become an important tool for meteorologists over the past 20 years. Radar can continuously scan an area about 200 km in radius day and night and in all weather conditions. The major limitation is that its field of view can be blocked by high terrain. Radar transmits pulses of radio waves to the targets, and receives the reflection from these targets and the range to the target is calculated from the Doppler shift in the signal. Radar calculates both the direction and distance to rainfall from the radar signal returning to the receiver. The “reflecting power” of the rainfall is correlated to rainfall intensity (Western Australia Server Weather Section, 2001).

Principles of Spatial Interpolation

Since rainfall stations cannot be located everywhere, spatial interpolation is an important method to determine average rainfall across rainfall stations. For a specified time period, average station rainfalls are calculated and contours (or iso-hyets) are plotted between them. There are many spatial interpolation methods, such as the Thiessen polygon, Kriging, thin-plate-splines and thin-plate smoothing splines. Each method has characteristics as described below.

The Thiessen polygon method assumes that the rain gauge is the best representation for the study area. This method sums areas from representative areas of equal rainfall defined around each gauge. These polygons are created by defining boundaries at a distance halfway between gauge pairs (Yang, 2001), and then joining them as the vertices. The result of this method is an isohyetal map of rainfall depth. Average rainfall is conventionally calculated between the contour lines by simple linear interpolation (Roberts and Hegland, 2000).

Roberts and Hegland (2000) present that this method gives equal rainfall regions with discontinuities between them. This assumption is often not justified and leads to consideration of the inverse distance-weighted methods, where rainfall estimates are weighted according to the distance between each rain gauge and the desired location. This results in a smooth rainfall distribution. Kriging and thin-plate-spline methods have the same desirable statistical property, but the disadvantage of Kriging and thin-plate-splines is that they do not scale linearly with the number of data points. The finite element-thin-plate method can be applied to one, two and three dimensional data. An additive-model is used to compute multi-dimensional data sets.

Loof (1994) designed rainfall networks by using Kriging methods. He analyzed the spatial variation structure of monthly and annual average rainfall and showed that Kriging can identify the optimum positions for a set of additional rain gauges by Kriging the standard deviation as an indicator. Biau *et al.* (1999) used the Kriging method to estimate rainfall in the empirical orthogonal function (EOF) space

of a sea level pressure field. In this research, a simple polygon method was compared with Kriging for estimating daily rainfall. The results show that Kriging is a better estimate of daily rainfall than a simple polygon method. Chegini *et al.* (2001) estimated rainfall using thin-plate smoothing splines (TPSS), with and without co-variable (TPSS-CO), weighted moving average (WMA), and Kriging (ordinary, co-Kriging and log-Kriging). The data represented 167 climatic stations in south-west Iran with 22 years of record. The results of this research show that the TPSS method is the most accurate method for simulating monthly and yearly rainfall.

Hancock *et al.* (2001) used thin-plate smoothing spline functions of position and elevation to interpolate 78 years of monthly mean rainfall for the Wet Tropics region. From the results, thin-plate splines have potential for estimating long-term mean rainfall in the Wet Tropics with a useful degree of accuracy.

In summary, the Theissen polygon is an easy method for the spatial interpolation of rainfall, because it uses a simple equation to determine the contour line of the rainfall. However, errors occur when rainfall stations are far apart, because the rainfall distribution may not be regular over the intervening distance. Therefore, this method is more suitable for areas where rainfall station density is high and for general water resources research. On the other hand, Kriging, thin-plate, and the thin-plate smoothing splines deliver more accurate estimates of rainfall distribution, but are more demanding than the Theissen polygon, because the geo-statistical computations to mimic natural rainfall distribution are intense. Since the solutions of these calculations are complex, the user has to spend a lot of time to understand the methodologies and to determine rainfall distribution. The appropriate choice of method depends on the application, the resolution of data, the time available and the experience of the researcher.

Rainfall Estimation using Remote Sensing

Remote sensing is a relatively new technology for rainfall estimation. There are many techniques which have been created to estimate rainfall. Most of them are

based on the detection of rain clouds and determining rainfall using a variety of more or less refined algorithms. The estimation of rainfall will be presented using visible, infrared and microwave channels. The wavelengths of visible, infrared and microwave are 0.4 to 0.7 mm, 0.7 mm to 3.0 mm, and 1 mm to 1 m, respectively. The visible bands contain the natural-color wavelengths. The infrared range has two categories based on their radiation properties, which are reflected infrared and the emitted or thermal infrared. Microwaves have the longest wavelengths used for remote sensing. The shorter wavelengths have properties similar to the thermal infrared region, while the longer wavelengths approach those used for radio broadcasts.

Principles of Microwave, Infrared, Visible Scattering and Cold Cloud Temperature

The classification of remote sensing techniques includes passive remote sensing and active remote sensing. Passive remote sensing comprises microwave techniques and visible and infrared techniques, while active remote sensing includes radar (e.g., TRMM radar).

Microwave sensing is attractive for rainfall calculation, because it can penetrate through cloud cover, haze, dust and all but the heaviest rainfall, as the microwaves are not susceptible to atmospheric scattering. The active microwave sensor is commonly radar, which transmits a microwave signal towards the target and detects the backscattered portion of the signal. The strength of the backscattered signal is measured to differentiate targets and the time delay between the transmitted and reflected signals is used to calculate the distance or range to the target. The reflected (backscattered) radiation is used to estimate rainfall rate, while integrating the rainfall rate over time yields accumulated rainfall. In theory, radar helps to continuously estimate the spatial variability of rainfall, because radar scans continuous regions. A radar signal which hits a cloud or rainfall can be scattered or absorbed, depending on the relative size of the wavelength in comparison to the object it strikes. Microwave radiation in clouds is mostly unaffected or only lightly

scattered, but it can be reflected by rainfall. X-band (wavelength is 1.5-2 cm) can be affected by extremely intense rainfall. C-band (5 cm) and L-band (25-28 cm) penetrate clouds and are not backscattered by rainfall or the cloud itself. Therefore, the required wavelength for rainfall detection lies close to the thermal wavebands and should be between a few mm and 1-1.5 cm. The microwave technique is based on interpreting the received signal's emission/absorption and scattering characteristics so that rainfall can be directly measured (Engman, 1995; Long, 1997; Milan, 1997; Seo, 1998; Laing *et al.*, 1999; Tait *et al.*, 1999; CCRS, 2002; Shao, 2002; CCFFWS, 2003).

Rain drops cannot be sensed directly using the shorter visible and near infra-red wavebands. These wavelengths are completely filtered by clouds, but cannot detect aerosols easily. However, the thermal band infra-red bands provide very good detection of cloud and aerosols (and are therefore used in cloud filtering and correction algorithms for the visible and NIR bands). The thermal band will of course give good estimates of the temperature at the top of a cloud. Thus, one needs to relate the independent measurements of rainfall to the properties of a cloud measured by infrared and visible remote sensing. Cloud temperatures are used for rainfall calculation. For the visible channel, clouds and the earth's surface are reflected in daytime because the light source is the sun. Thicker clouds generally have higher reflectivity, so they are bright in visible imagery. The land surface reflects sunlight less than clouds, but more than the sea surface. For the infrared channel, clouds and the earth's surface reflect in this channel, and the intensity of radiance depends on the temperature of the radiation source. The higher the temperature, the more intense the infrared radiation. High clouds are invariably very cold, while low clouds are much warmer (Costulis, 2002). So, the intensity of the infrared radiation in this channel can infer both the temperature and the height of the cloud top.

Clouds can be classified by shape, content or cloud height. There are two basic shapes of cloud - stratus and cumulus. The characteristic of a stratus cloud is being layered or sheet-like, while a cumulus cloud is puffy and heaped. Cloud height can be classified in three levels - high, middle, and low (Costulis, 2002; Tatsuo,

2003). More comprehensively, Cloudmans (2002) provides twelve basic cloud classifications as shown in Table 6.

The temperature of the atmosphere above the Earth decreases with altitude, at a rate of - 7 degrees Celsius per kilometer. A cloud's altitude is given as "ceiling", which is the measurement at the top of a cloud and is part of the set of upper air measurements (Van der Meulen, 2002). Table 7 presents the relationship between cloud height and cloud temperature.

After the satellite measures the temperature of clouds, the temperature in the satellite image is represented by various shades of gray. Whiter areas are the coldest part, while darker areas are the warmest part. The apparent temperature of clouds depends on many factors that include cloud height, its size and make-up of the particles that form the cloud (NASA, 1998).

Microwave radar is suitable for forecasting rainfall over short time periods and the measurement of rainfall when it's raining, since the microwaves backscatter from both cloud and rainfall. On the other hand, infrared and visible are convenient for forecasting rainfall, because they can measure both temperature and height of cloud. Both the cloud temperature and the cloud height are determined to forecast when and where rainfall can occur.

Table 6 Twelve basic cloud classifications

Cloud Type	Cloud Height (m)	Description	Family
1. Cumulus Congestus	>7,600 (top) 1-1,800 (base)	Very active separated heaps with flat bottoms and growing towers	Cumulus (Heap) Family
2. Swelling Cumulus	4-7,600 (top) 1-1,500 (base)	Active separated heaps with flat bottoms and bumpy cauliflower tops	Cumulus (Heap) Family
3. Cumulus of Fairweather	1-1,500 (top) 0.5-900 (base)	Small heaps of clouds with flattish bottoms and rounded tops	Cumulus (Heap) Family
4. Cirrostratus	>7,600	High level veil of ice crystal cloud, frequently producing a halo around Sun or Moon	Stratus (Layer) Family
5. Altostratus	5-6,100	Thickly layered water droplet cloud. Sun's disk diffused as viewed through sheet of ground glass	Stratus (Layer) Family
6. Stratus	0 – (Fog) 0.5-2,500	Low-lying formless cloud, called fog when base lies on the ground	Stratus (Layer) Family
7. Cirrocumulus	>7,600	High level layered cloud with wavelike or fine, dappled cumuliform structure	Heap/Layer Family

Table 6 (cont'd)

Cloud Type	Cloud Height (m)	Description	Family
8. Altocumulus	4-6,100	Mid-level layered cloud with globular structure, sometimes called "buttermilk sky"	Heap/Layer Family
9. Stratocumulus	1-3,000	Low layered cloud with bumpy, heap-like structure	Heap/Layer Family
10. Cirrus	>7,600	An ice crystal cloud showing filaments of ice crystals precipitating and evaporating	Precipitation Family
11. Cumulonimbus	>7,600 (top) 1-1,800 (base)	A massive pile of cloud penetrating the freezing level and sometimes forming an anvil at the base of the stratosphere	Precipitation Family
12. Nimbostratus	3-7,600	Generally formless dark mass of low storm cloud associated with general continuous rainfall or snowfall	Precipitation Family

Source: Cloudmans (2002)

Table 7 Relationship between cloud height and cloud temperature

Cloud Height (meters)	Temperature (^{0} Celsius)
0	15
1,250	8
2,500	-1
3,750	-6
5,000	-13
6,250	-24
7,500	-34
8,750	-41
10,000	-50
11,250	-57

Source: Van der Meulen (2002)

The Nature of Rainfall in the Temperate Zone and the Tropical Zone

The Earth has three climatic zones - polar, equatorial, and the mid-latitude zone. In the polar zone (60^0N to 90^0N and 60^0S to 90^0S), temperatures are below freezing all the time and very dry. This zone is bitterly cold. The climate in the equatorial zone (30^0N to 30^0S) is always hot and usually rainy. The tropical zone ranges between 23.5^0N to 23.5^0S of the equator. The tropical zone experiences small temperature changes, both daily or seasonally. The climates in the mid-latitude zone or temperate zone (30^0N to 60^0N and 30^0S to 60^0S) are those without extremes of temperature and rainfall and are in between the polar zone and the equator zone. The climate in this zone can be presented by three sub-zones. First, climates are wet, with cold winters and hot summers on the east coasts of continents. Second, climates are dry, with even colder winters and hotter summers in the interior parts of continents. Last, climates are mild with rainy winters and dry summers on continental west coasts (Washington and Todd, 1999; Costulis, 2002; Srinivasan, 2002; Senges, 2003).

Patterns of rainfall change with season, latitude, and the movement of the sun. In temperate zones, the annual rainfall is some 100 inches or 2,500 millimeters on western facing coastlines, and decreases within the interiors of major landmasses. The tropical zone, which has strong heating from the sun, has the highest rainfall. Two-thirds of global rainfall occurs in the tropical zone, so this zone has great importance for the global hydrological cycle. The process of rainfall, which releases the latent heat of condensation, transfers heat energy to the atmosphere. Three-fourths of the atmosphere's heat energy comes from the tropical zone. The total of average annual rainfall is usually more than 100 inches or 2,500 millimeters, and can increase to 400 inches or 10,000 millimeters if it is influenced by the monsoons.

In the eastern portion of tropical oceans, there are many tropical storms that track westward. Hurricanes, typhoons and willy-willy all start out as weak low pressure areas those form over warm tropical water. Tropical storms have wind speed ranges from 17.43 m/s to 32.63 m/s. The hurricane has wind speeds that equals or exceeds 33.08 m/s. A hurricane is called a typhoon in the western Pacific, while it is called a cyclone or willy-willy in the water around Australia (ARIC, 2003; NASA, 2003).

Satellite Sensors

In this section the available sensors / satellites are decribed: Meteosat, GMS, and TRMM. These satellites are meteorological satellites, which can determine rainfall by direct and indirect measurement of rainfall.

The Meteosat Satellite

Meteosat is a geostationary satellite, which is located 36,000 km above the intersection of the Equator and the Greenwich Meridian. The Meteosat family has seven satellites, of which Meteosat 1, 2, 3, and 4 are no longer in service. Meteosat 6 is mainly used, while Meteosat 5 is kept as a standby craft. The latest satellite of the same design, Meteosat Transition Program (MTP), was launched in 1997 and was

used until the start of the Meteosat Second Generation operation in 2000. The satellite spins at 100 rpm about its main axis that is nearly parallel with the Earth's North-South axis. The period of this orbit is 24 hours, which is equal to the orbit of the Earth.

The main sensor on board Meteosat has three high-resolution spectral bands as shown in Table 8. The visible spectrum is used to indicate the surface albedo (reflectance), and the image resembles that of a normal photograph. The infrared (thermal) is used to indicate the energy of radiation from the surface and cloud tops, so the images present surface temperature and cloud top temperature. Rainfall is determined by correlation of cloud top temperature as CCD (Cold Cloud Duration) and measurements of actual rainfall at the ground. The infrared (water vapour) or Mid-IR band is used to indicate the total water present in the atmospheric column.

Table 8 The three spectral-bands of Meteosat

Spectral-bands	Wavelength (μm)	Resolution at Nadir
Visible	0.4-1.1	2.5 km
Infrared (Water vapour) or Mid-IR	5.7-7.1	5 km
Infrared (Thermal)	10.5-12.5	5 km

Source: NASA (2006)

The fourth channel is a radiometer, the Multispectral Imaging Radiometer (MIR), which scans the earth's surface line-by-line in an east-west direction. The visible channel scans 5,000 lines, with each line including 5,000 pixels, and the infrared channels scan 2,500 lines, with each line comprising 2,500 pixels. The visible and infrared are converted into analog electric signals by five detectors that are two visible and three infrared. These detectors are distributed across the focal plane of the radiometer. Instantaneous field-of-view (FOV) at the Earth's surface (2.5 km^2) of the two visible detectors is determined by their physical size (250 x 250 micrometers sensitive area), while each infrared detector is 70 square micrometers

and creates an instantaneous FOV 5 km^2. Thus, the resolutions of images are 2.5 km and 5 km, respectively. The radiant energy of the different spectral bands is measured in each radiometer pixel. This measurement is digitally coded and transmitted to the ground station.

During an image scan, different image lines appear due to the satellite's rotation around its vertical axis (100 revolution per minute), and for the duration of the next revolution the radiometer is tilted somewhat, so that the next line further north comes into the field of view. The telescope is made to scan through 18 degrees in the south-north direction, giving a full scan every 25 minutes. For the completion of the scan, the telescope returns to its starting position, which takes 5 minutes so that the next scan starts after 30 minutes. Thus, Meteosat images are taken in half-hourly intervals (ESA, 1997; Marchant, 1998; Cresswell, 2003).

Geostationary Meteorological Satellite (GMS)

GMS is another geostationary satellite, which is located above the earth's surface 36,000 km, and over the equator at 140^0E, north of Australia. The orbit period is the same as the rotation of the earth. A geostationary satellite views the same geographic area either day or night because the field of view of the geostationary orbit is fixed and allows regular sequential observations of cloud pattern over a defined region using visible and infrared radiometers. GMS has an Asian coverage, whilst Meteosat has a European and African coverage.

GMS-5, launched in 1995, is the present spacecraft. This spin-stabilized satellite senses both visible radiation reflected from the Earth (or cloud), and infrared radiation emitted by the Earth, clouds, and atmosphere. GMS-5 has four channels to observe the Earth as shown in Table 9. Channel 1, or the visible channel, is used to provide high resolution visible imagery. The visible image can be used to identify low-lying clouds, which are usually invisible at infrared wavelengths, but can only be observe a during daylight hours. Channel 2, or the infrared channel, is used to indicate the temperature of clouds and the surface. Channel 3 is similar with Channel

2. Lastly, Channel 4, or the water vapor channel, is used to observe emissions from water vapor in the atmosphere.

Table 9 Description of GMS channels

Channel	Spectral Interval (mm)	Ground Resolution (km)
1 (Visible)	0.5 – 0.75	1.25
2 (Infrared)	10.5 – 11.5	5
3 (Infrared)	11.5 – 12.5	5
4 (Water Vapour)	6.5 – 7.5	5

Source: NASDA (2003)

Normally, the observation hemisphere of GMS-5 is every hour, but it observes every 30 minute during the synoptic hour. Since the synoptic hour is an hour in which each meteorological satellite such as GMS and Meteosat collect an overall view data, GMS has to collect more data than at the other times. This satellite scans the earth surface from north to south in a series of lines over a period of 22 minutes. Each observation consists of some 10,000 lines of visible, and 2,500 lines of infrared data (Johnson, 1996; CSRSR, 2003; NIWA, 2003; NASDA, 2003).

Tropical Rainfall Measuring Mission (TRMM)

TRMM is the first satellite used to measure rainfall in tropical and subtropical areas by using microwave and visible infrared sensors. It houses the first spaceborne rainfall radar. The objectives of this satellite are:

- to collect and study, for multi-year science data sets, measurements of rainfall in the tropical and subtropical zone;
- to understand how interactions between the sea, air and land masses produce changes in global rainfall and climate;

- to improve modeling of tropical rainfall processes and understand their influence on global circulation in order to predict rainfall and variability at various time scale intervals; and
- to test, evaluate and improve the performance of satellite rainfall measurement techniques.

TRMM's orbit is circular, non-sun-synchronous, and at an altitude of 350 km. This orbit is located over a range of latitudes between 35 degree north and 35 degree south. It can view each position on the Earth's surface at different local times each day. Thus, TRMM produces a data set vastly more informative than any previously available.

TRMM has three instruments in its rainfall measurement package: the TRMM Microwave Imager (TMI); the Precipitation Radar (PR); and the Visible Infrared Scanner (VIRS). The characteristics of the TRMM instrument are shown in Table 10. The TRMM Microwave Imager (TMI) is used to provide information on the integrated column precipitation content, cloud liquid water, cloud ice, rainfall intensity and rainfall type. The Precipitation Radar (PR) is the first radar specifically designed for monitoring rainfall that operates from space. PR is used to measure the distribution of rainfall over both the land and ocean and to define the layer depth of precipitation. The Visible Infrared Scanner (VIRS) is used to provide high resolution observations on cloud coverage, cloud type and cloud top temperature.

During each orbit, TRMM satellite data are stored on board and transmitted to the ground via the TDRSS (Tracking and Data Relay Satellite System). The TRMM science data are processed into standard production by TSDIS (TRMM Science Data and Information System), and these products are transferred to the Goddard DAAC (Distributed Active Archive Center) for archival and dissemination (Kummerow *et al.*, 1998; Bolen and Chandrasekar, 2000; Kummerow *et al.*, 2000; NASA, 2003; Lawrence, 2003).

Table 10 Characteristics of the TRMM instrument

	Frequency/wavelength	Scanning Mode	Ground resolution	Swath Width
TMI	10.65, 19.35, 37.0, 85.5 GHz dual polarization, 22.235 GHz vertical polarization	Conical	Ranges from 5 km at 85.5 GHz to 45 km at 10.65 GHz	760 km
PR	13.8 GHz horizontal polarization	Cross track	4.3 km at nadir	220 km
VIRS	0.63, 1.6, 3.75, 10.8, 12 μm	Cross track	2.1 km	720 km

Source: NASA (2003)

Estimation of Rainfall using Ground-Based Data and Remote Sensing

The TRMM satellite uses visible, infrared and radar channels to estimate rainfall, while Meteosat and GMS use visible and infrared channels. None of these satellites will measured rainfall directly, so satellite-based rainfall estimation algorithms must be calibrated using direct observations. Although rain gauges observe rainfall directly, they only represent point rainfall, but this is still considered to be close to 'true' rainfall. This is the main reason why rain gauge-based estimates of rainfall are used for validation of satellite-based rainfall quantities.

Meteosat's TIR images are used to measure cloud-top temperature. Cold-Cloud-Duration (CCD) is defined as the time that a given pixel remains below a threshold value. CCD is assumed to be linearly related to rainfall, and is reasonable for cumulonimbus clouds associated with convective rainfall. When there are significant amounts of cirrus clouds (cold clouds with no rain) or frontal stratiform clouds (warm clouds with rain) this linear relationship is not correct. Rainfall over each pixel in the satellite image is estimated from this linear relationship, and then the

rainfall map is created from the thermal infrared imagery. Rain gauge data in the same area of the satellite image is estimated by using an interpolation method, such as Kriging, and then the rainfall map from rain gauge data is created. The rainfall map from thermal infrared imagery is compared with the rainfall map from rain gage data to calibrate the volume of rainfall (Thorne *et al.*, 2001).

The GMS satellite determines rainfall from a non-linear equation ($P = aT^b$), where T is cloud top temperature (K) and P is rainfall (mm). Cloud top temperature can be estimated from GMS satellite images, while rainfall can be determined from ground-based measurement. In the target area, cloud top temperature and rainfall are collected, and they are plotted to find the **a** and **b** coefficients. Then, the equation between P and T is created for each characteristic area. This equation is used to predict rainfall in that area when cloud top temperature is determined from GMS satellite imagery. The confidence of this equation can be defined from the coefficient of determination, or r^2 . The selected a and b parameters have importance for the accuracy of the created equation. In addition to the a and b parameters, P and T are also significant, because all of these parameters have an influence on the coefficient of determination (Udomchoke and Aungsuratana, 1995).

There are many methods for the estimation of rainfall using radar data from TRMM satellite imagery, for example the Z-R relationship, R(Kdp), and R(Kdp,Zdr). The details of these methods are presented below (Atlas, 1997; Ciach *et al.*, 1997; Braga and Massambani, 1997; Kolb and Matt, 2000; Gorgucci *et al.*, 2001).

The Z-R relationship is the proportion between radar-measured reflectivity (Z) and rainfall rate (R), where the Z-R relationship can be represented by $Z = aR^b$. Coefficients **a** and **b** must be estimated in the first step and the Z-R relationship is different for various regions and precipitation types. Even with the same kind of precipitation, the Z-R relationship can change from time-to-time because of the variation of the shape of the drop size distribution. The definition of drop size distribution is described by the following equation:

$$N_d = N_o \exp(-\lambda D) \tag{61}$$

where N_d is the number of drops per cubic centimeter, N_o is equal to 0.08 cm^{-4} for rain from stratiform clouds, λ depends on the rain intensity and is expressed in units of per millimeter, and D is the drop size diameter (Battan, 1973). The drop size distribution can theoretically model rain reflectivity using the wavelength parameters of the radar and the known backscattering properties of liquid water spheres.

R(Kdp) is a function of rainfall rate and specific differential phase (Kdp). The specific differential phase (Kdp) can be used to calculate the rainfall rate using polarimetric radar. The specific differential phase (Kdp) can be calculated by the following equation:

$$Kdp = \frac{1}{2}\left(\frac{d}{d_r}\right)(phi\_dp) \tag{62}$$

where phi_dp is the measured differential phase between the horizontal and vertical pulses. Since the specific differential phase (Kdp) is also related to the drop size distribution, the equation of the drop size distribution is shown as follows:

$$N_d = N_o D^n \exp\left[-(3.67+n)\frac{D}{D_o}\right] \tag{63}$$

where N_d is the number of drops per cubic centimeter of size range, N_o is equal to 0.08 cm^{-4} for rain from stratiform clouds, D is the volume equivalent spherical diameter, and D_o is the median volume diameter of the distribution.

The relationship between rainfall rate and the specific differential phase (Kdp) for various drop size distributions can be accomplished using the following equation.

$$R = 40.56 Kdp^{0.866} \tag{64}$$

R(Kdp,Zdr) is a function of rainfall rate, specific differential phase (Kdp), and differential reflectivity factor (Zdr). The relationship of R(Kdp,Zdr) can be estimated from the following equation (Jamison, 1991).

$$R = 52.0\left(Kdp^{0.96}\right)\left(Zdr^{-0.447}\right) \tag{65}$$

The estimated rainfall using a simple Z-R relationship is suitable for storms without hail, so the Z-R relationship helps to calculate rainfall in simple conditions. However, many extra-tropical thunderstorms consist of hail cores, which have much higher reflectivity than liquid rain shafts, and this means that Z-R relationship will overestimate rainfall because of the higher reflectivity of hail. On the other hand, the specific differential phase (Kdp) is suitable for the estimation of rainfall that includes hail because this method is less affected by hail. However, the specific differential phase (Kdp) has poor spatial resolution. To solve this problem, rain-rate relations utilizing (Kdp, Zdr) are used, although this does not properly deal with hail contamination in Zdr.

The overall methodology of radar-rainfall estimation can be summarized in the following steps. In the first step, the raw data are processed, using the system parameter file and appropriate corrections are made for attenuation. Second, a radar reflectivity map is created, and the echoes are classified into convective and stratiform classes. Third, the radar reflectivity above a specified threshold, which might be distinct for different rain regimes, is vertically integrated and the integral is converted into rainfall estimates using the nonlinear regression relationships. The detail of the relationships varies for convective and stratiform and use continuous distance from the radar as another predictor. Fourth, the rain rate in polar coordinates is transferred onto a Cartesian grid. The velocity vectors of rainfall pattern are calculated by using cross-correlation, and then an hourly accumulation map is created. The accumulation maps of 1-day, 10-days, monthly, and so on are created. Fifth, the available rain

gauge data is considered, and the average monthly residual bias is calculated. Sixth, the adjustment of mean field bias is operated. Rainfall patterns, which are integrated in time to express the accumulation of rainfall, are adjusted to the rain gauge-based real average of corresponding rainfall. In the adjustment, sampling error of typically sparse rain gauge networks should also be accounted for. The adjustment factor can be used to adjust radar when it forecasts in a time period following calibration and prior to arrival of new rain gauge observations. In the final step, rain gauge observations may be used to locally adjust radar-rainfall patterns by using optimal merging of the two sets of rainfall estimates according to some performance criterion (e.g. minimum error variance).

Some experts have questioned the accuracy of TRMM in predicting rainfall from tropical storms. They note that the majority of rainfall occurs in the build-up period of the storm and decreases in the second build-down phase. Since many storms are less than three hours in duration, they may not be correctly observed by TRMM, as its repeat pass sampling is every 91 minutes or more (Chandrapala, Sri Lanka Dept. of Meteorology, 2002).

Ground-based radar can measure rainfall information at spatial and temporal scales suitable for such applications. This requires three parts to work: (1) an antenna or receiver; (2) computers that process the raw radar data; and (3) an interactive workstation the forecasters can use to display the processed radar data. Ground-based radar detects information at different scanning elevations and patterns, in addition to varying pulse frequencies. Radar sends out a pulse, and listens for a return signal. The return observed in a radar sounding will be computed from the shape of the radar antenna, the wavelength, frequency and energy transmitted. Radar based reflectivity images are normally presented by color in dbZ, which is a logarithmic scale of the target's reflectivity. The reflectivity, which is received by radar, can present precipitation type, storm physics, and a good sense of the intensity of storm patterns. The properties of a Z-R relationship relates to the reflectivity of radar, so this relationship is also suitable for analysis of rainfall using ground-based radar (FAS, 2003; Nichols, 2003; NWS, 2003).

Rainfall Measurement using Ground-Based Data and Remote Sensing in Thailand

The rainfall in Thailand is tropical, so annual average rainfall is more than 1,000 mm. In the rainy season, floods occur over large areas of Thailand because of heavy rainfalls. The duration and volume of heavy rainfalls are often unknown. Flood forecasting has not been implemented for the whole area of Thailand, so flood damage can be high in some areas. For this reason, rain gauges should cover all of Thailand and should have high efficiency for rainfall estimation. Remote sensing technology can play a key role in improving rainfall estimates.

Presently, rain gauges are usually used in Thailand to measure rainfall, while remote sensing technology is used to detect meteorological information for weather forecasting. Thailand is trying to use remote sensing technology to estimate rainfall, but it is difficult because both expensive equipment and high technology are required. Also, it is not easy to find specialists in this field.

Daily rainfall is measured by the Thailand Meteorological Department (TMD), Royal Irrigation Department (RID), and Royal Forest Department (RFD) (Agata, 2002). RID and RFD normally uses rain gauges, while TMD uses rain gauges to measure rainfall and uses remote sensing technology to collect meteorological information. The equipment used at a climate station includes: Thermometer screen, Maximum-Minimum Thermometer, Dry-Wet Bulb Psychrometer, Thermo-Hygrograph, American Class A Evaporation Pan, and Rain gauge. Many rainfall stations have some of these instruments as well.

TMD uses ground-based radar and a meteorological satellite. For ground based radar, X-Band, C-Band, and S-Band are used to measure the intensity of rainfall. The frequencies of these bands are 6,200-10,900 MHz, 3,900-6,200 MHz, and 1,550-3,900 MHz, respectively. The wavelengths of these bands are 2.75-4.84 cm, 4.84-7.69 cm, and 7.69-19.3 cm, respectively. TMD's ground-based radar stations are located in Chiang Rai, Mea Hong Son, Chiang Mai, Phitsanulok, Sakon Nakhon, Khon Khaen, Ubon Ratchathani, Surin, Don Muang, Rayong, Hua Hin, Sum Porn,

Surat Thani, Phuket, Ranong, Trung, Song Kha, Nara Thiwas and Thailand Meteorological Department. There is also a mobile radar unit. These stations nearly cover all of Thailand. Ground-based radar is used for air transportation and weather forecasting. It is measured every hour during regular weather conditions and every 30 minutes in unusual weather conditions. It can determine rainfall intensity, cloud movement, and the location of rainfall (TMD, 2001).

Meteorological satellites, which are used by TMD, include GMS-5. This satellite is used for meteorology information by remote sensing and direct broadcast, such as cloud top temperature, cloud movement, temperature, sea surface temperature, Earth surface temperature, radiation from sun, moisture, ozone, and transfer information to members or users. The bands of GMS 5 include the water vapour band (6.5 – 7.0 micron), and the infrared band (10.5 – 11.5 and 11.5 – 12.5 micron (TMD, 2001).

Udomchoke and Aungsuratana (1995) used cloud top temperature from GMS 4 and rainfall from ground-based rainfall stations (20 stations) to calculate a non-linear regression equation of relationship between cloud top temperature (T) and rainfall (P) in Northern Thailand. The equations are $P = 4.3932 \times 10^{58} T^{-24.80}$ (r^2 = 0.97) in the dry season (March – May 1993), and $P = 1.8462 \times 10^{22} T^{-8.93}$ (r^2 = 0.62) in the rainy season (August – September 1994).

Saovaphak (1996) used GMS S-VISSR RECEIVER/DC and ground-based rainfall to estimate rainfall based on the relationship between rainfall amount (P) and cloud top temperature (T) in terms of a non-linear regression equation. The equations for Northern, Northeastern, Eastern, and Southern Thailand from January to December 1994 are: $P = 1.1102 \times 10^{13} T^{-4.8288}$, $P = 4.4905 \times 10^{10} T^{-3.8012}$, $P = 5.2384 \times 10^{12} T^{-4.6683}$, and $P = 2.4916 \times 10^{11} T^{-4.0840}$, respectively, with coefficients of determination (r^2) being 0.71, 0.73, 0.70, and 0.71, respectively.

Water Budget

Principal of Water Budget

The process of water budget concerns the natural water cycle in a particular area and compares the availability of water to amount of water that is used and withdrawn in that area. When conducting a water budget, it is very important to understand the connection between the area's ground and surface water. In water cycle, water is evaporated from the land and ocean by the latent heat and the water vapor rises. Thereafter, it condenses into clouds and they will be rain. The rain hits the ground and part runs off, part infiltrates into the ground, and part evaporates back up into the sky. The water from soil will be taken by the plants and vegetation and the water will be released into the air through transpiration. Other parts of the ground water enter streams and flows onto the surface. Eventually, the surface water that runs off in streams, towards the ocean, will be evaporated and continued the cycle. (Molden, 1997; Natalia et. al, 2004)

The water budget is an accounting of the inflow, outflow, and change in storage of water. The water budget of place, whether it be an agricultural field, region, or continent can be calculated by computing the inflow and outflow of water. The major inflow of water is from rainfall and outflow is evapotranspiration (Ritter, 2001; Fujiki *et al.*, 2000). The water budget may be expressed as a simple equation (Cresswell, 2000; Dominguez, 2000; NSF, 2003; WRA, 2003):

$$\text{Inflow} = \text{Outflow} + \text{Change in Storage} \tag{66}$$

Addition, the appropriate degree of sophistication in the equation of water budget depends on the purpose of the analysis and on the complexity of the system. For example, if the purpose is to obtain a groundwater control system or a flood disposal system or to understand the effects of surface water quality and quantity and soil salinity, detailed and specialized modeling may be required (Perry, 1996). Molden (1997) classifies the level of calculation into field, irrigation service, and

basin level and presents the component of inflow, outflow, and change in storage for each level as Table 11.

Water Budget Calculation in Thailand

In Thailand, the main equation for water budget calculation is also that inflow equals to outflow minus change in storage. Inflow is mainly rainfall while outflow is mainly evapotranspiration. The detail and specific values of inflow and outflow are based on the complexity and level of study area as Table 11. The followings are the example of experience for water budget computation in Thailand.

Tangtham (1994) studied the influence of forests and forest conversion on stream flow and water consumption. Theoretically, watershed hydrological behavior, such as streamflow and sediment discharges, is dependent on the types of watershed cover and the geomorphological and pedological setting. For this research, the water consumption of forest and tree plantations was investigated by using water balance equations and by measuring transpiration rates. The evapotranspiration loss estimated by water balance indicated that almost all types of forests in Thailand consume more than 1000 mm/year of water if annual rainfall is not inhibited by drought.

Molle *et al.* 2001 used the concept of water budget to prepare the water accounting for the Chao Phraya Delta. The main components for this study consist of water released from dam, side flows, diversion to agricultural areas, rainfall, return flows, inflow from adjacent rivers, exchanges with the aquifer, water released from the flood-prone area, crop consumptive use, inland navigation, domestic use, evaporation in waterways, pollution control, salinity control, and water flowing to the sea. The result is the diagram of water accounting for the study area that presents water in Billion m^3 for each component.

Petvirojchai (2004) determined the monthly mean evapotranspiration in Northeastern region of Thailand. Thereafter, the main concern of the following study is to have realistic estimations of monthly evapotranspiration for water budget

computations in case of dangerous water surplus (flood) situations. The method to obtain water budget calculation by Thornthwaite method is the relation between rainfall, potential evapotranspiration, runoff, and change of soil moisture storage. The result of water balance calculation presents that the water surplus in the Northeastern region is occurs during the time between June to September and the maximum water surplus is 1314 mm./year.

Sombat *et al.* (2004) applied the concept of water budget to study the changes of phreatic surface in natural groundwater recharging area corresponded by fluctuating of flood levels in a large floodplain in the Yom River Basin in Phichit Province in Thailand. The main inflow and outflow used in this research are consist of rainfall, water level, phreatic surface level at each observation well, and losses of surface runoff by infiltration and percolation. The result of this research shows that thr phreatic surface levels in 2001 and 2002 were raised up but the phreatic surface in 2003 was recessed with lower with lower than in 2001 and 2002, respectively.

Tsubo *et al.* (2004) determined percolation rate and the lateral water flow (seepage) using the water balance equation with reference to the toposequential variation of sloped lowlands. The study areas are in Chum Phae (16°32′N, 102°7′E), Khon Kaen (16°25′N, 102°48′E), Ta Pra (16°19′N, 102°49′E), Phimai (15°14′N, 102°28′E), Surin (14°54′N, 103°30′E) and Ubon Ratchathani (15°19′N, 104°40′E), which are located in the northeast, during the 2000 season. The water balance equation represents the relationships among rainfall, runoff, percolation, seepage, evaporation and transpiration. Therefore, if the change in free water level is known, the total amount of percolation and seepage can be determined. If percolation is independently determined, seepage can be then computed. The result presents that percolation rate determined in this study agrees with the previously reported values. The maximum values of the lateral water flow were very high, and a similar result was previously reported.

Table 11 Water budget components at field, irrigation service, and basin level

Field Level	Irrigation Service Level	Basin Level
Inflow		
- irrigation application	- surface diversions	- precipitation
- precipitation	- precipitation	- trans-basin diversion
- subsurface contribution	- subsurface sources	- groundwater inflow
- surface seepage flow	- surface drainage sources	- river inflow into basin
Outflow		
- crop transpiration	- crop transpiration	- crop transpiration
- evaporation from soil surface	- evaporation from free water and soil surfaces, weeds, phreatophytes, and other non-crop plants	- municipal and industrial uses
- weed evapotranspiration		- fisheries, forestry, and other non-crop depletion
- lateral flow to salt sink		- dedicated environmental wetlands
- flow to sink	- flow to sink	- evaporation from free water and soil surfaces, weeds, phreatophytes, and other non-crop plants
- water rendered unusable due to degradation of quality	- evaporation from ponds	- evaporation from ponds
- deep percolation	- water rendered unusable due to degradation of quality	- flow to sink
- seepage	- stream commitment	- water rendered unusable due to degradation of quality
- surface runoff	- downstream commitments	- evapotransporation natural vegetation
	- M&I use within irrigation service	- stream commitment
	- uncommitted outflow	- downstream commitments
		- outflow commitments to maintain environment
		- uncommitted outflow

Table 11 (cont'd)

Field Level	Irrigation Service Level	Basin Level
Change in Storage		
- soil moisture change in active root zone	- soil moisture change - reservoir storage change - groundwater storage change	- soil moisture change - reservoir storage change - groundwater storage change

Source: Molden (1997)